A computational approach to model dynamic contact and fracture mode transitions in rock

Reza Abedi[a,1], Philip L. Clarke[b]

[a] *Associate professor, Department of Mechanical, Aerospace and Biomedical Engineering, The University of Tennessee at Knoxville/Space Institute, TN, USA*
[b] *Formerly at the Department of Mechanical, Aerospace and Biomedical Engineering, The University of Tennessee at Knoxville/Space Institute, TN, USA*

Abstract

We propose an interfacial contact and fracture model based on Riemann solutions. Instead of penalty method and Lagrange multiplier approach we propose a regularization scheme—based on the interface displacement and separation velocity jumps—that smoothens contact-separation mode transitions. An aperture-based regularization approach smoothens the transfer of hydraulic load to in-situ cracks. A discontinuous Galerkin implementation is used to solve dynamic fracture problems for uniaxial compression and explosive examples. Moreover, we investigate contact–separation mode transitions and hydraulic load transfer in several hydraulic refracture problems and study the effect of loading rate and in-situ cracks in the number and orientation of activated perforations.

Keywords: contact fracture transition, dynamic fracture, Riemann solution, crack intersection, hydraulic refracture, Spacetime discontinuous Galerkin

1. Introduction

Given that rocks are often under confinement pressure, contact and friction play a critical role in rock mechanics. As discussed in [1], except a limited cases where fracture is mostly tensile driven, rock fracture can be considered as a consequence of tensile and shear *micro-fractures*. Specifically, for brittle hard rock macroscopic fractured are formed by gradual closure, initiation, propagation, and coalescence of these microcracks [2, 3]. During such complex crack propagation processes, contact mode transitions are frequent even for the simplest loading conditions. For example, for uniaxial compressive loading crack propagations may initiate from local stress concentration points in tensile mode [4], whereas shearing mechanisms become important after sufficient micro-tensile damage accumulation [5, 6]. Thus, modeling crack propagation in tensile and

*Corresponding author. Email: rabedi@utk.edu

frictional modes and the transition between various contact modes is of utmost importance in rock fracture.

Moreover, there are several examples of contact mode transitions in the area of hydrocarbon reservoir characterization and stimulation. In hydraulic fracturing the interaction of a hydraulically loaded crack with in-situ cracks can result in various mode transitions for both cracks. Some of these interactions are studied in [7, 8, 9, 10] The fluid flow can also be diverted into the in-situ crack, in which case it experiences a contact to separation mode transition.

The inverse of the aforementioned mode transition, *i.e.,* separation to contact mode transition, occurs in the initial stage of fluid flow application [11] or when the hydraulic load is released and crack surfaces are pulled back together. Understanding this transition, and the transition back to separation mode due to the re-application of hydraulic load becomes important in refracting applications; for example, in pump-in/shut-in and pump-in/flow-back tests [12, 13, 14], mini-hydraulic fracturing injections are performed wherein the hydraulic pressure is released after induced crack surfaces open. By recording *bottom hole pressure* (BHP) and repeating this test multiple times, until a constant fracture closure pressure is reached, the minimum principal in-situ stress of the rock formation can be measured. Cyclic application of the loads that better stimulate a reservoir, as in [15, 16], or re-fracturing a reservoir to reactivate hydraulic cracks or increase its productivity, *cf.* [17], and explosive fracturing [18, 19, 20] are some other applications that involve contact mode transitions.

Specific combined tensile fracture and contact models have been incorporated into different types of numerical methods for rock failure analysis. For example, the *discrete element method* (DEM) [21] and the closely related *grain-based model* (GBM) [3] implementations represent rock as a collection of (deformable) particles that interact through their boundaries by carefully designed models that include all contact and fracture modes. There have also been several approaches that combine different computational approaches to maximize their flexibility in modeling complex rock media. For example, [22, 23, 24, 10] proposed a combined finite-discrete element method (FDEM) and [25] proposed the *No Binary Search* (NBS) algorithm in which the contact detection algorithm favorably scales linearly with respect to the number of distinct elements. This approach was extended to hydraulic fracturing problems in [26, 27] to model contact mode transitions.

Aside from the particular form of interface contact / fracture model, the penetrability condition is enforced by different approaches. The most common numerical techniques include *penalty methods* [28, 29] and *Lagrange multiplier methods* [30, 31]. For example, a penalty method is used in [32]. In the context of rock mechanics and hydraulic fracturing, [16, 33] use the cohesive model approach to represent fracture processes on crack surfaces. To model contact, the former employs a penalty method while the latter enforces the contact condition by using a Lagrange multiplier approach. The hydraulic crack closure condition has also been modeled by using a nonlinear elastoplastic approach in [34]. Regarding the performance of these methods, it is noted that penalty methods allow an unpredictable amount of interpenetration and can generate

stiff, ill-conditioned systems that might require extremely small time steps for stability [35]. While Lagrange multiplier methods exactly enforce the impenetrability constraint, they may increase problem size or introduce a more complex computational framework.

In this manuscript we present a contact-fracture model that combines dynamically consistent *Riemann solutions* for separation, contact–stick, and contact–slip modes. It is emphasized that first unlike the aforementioned works in rock mechanics these solutions are formulated for dynamic, rather than static, failure analysis. Second, this contact model remedies the uncontrollable penetration of penalty methods by providing a maximum tunable penetration without resulting in a stiff system of equations. Third, as discussed in §2.2.4, no numerical regularization is required for contact stick–slip transitions. A uniaxial compressive loading test and a explosive loading of a wellbore are presented to demonstrate the ability of the aforementioned method in capturing various contact/fracture modes. The powerful adaptive operations of the *asynchronous spacetime Discontinuous Galerkin* (aSDG) method [36] is used to accurately solve the corresponding dynamic problem and represent the resulting complex fracture patterns.

These dynamic Riemann contact solutions were first presented in [37]. However, in their original form they cannot be applied to hydraulic fracturing applications as they do not correctly model contact–stick to separation mode transitions. In the present work, we propose a new regularization approach in the two dimensional phase space of normal separation and normal separation velocity jump that remedies this problem, *cf.* §2.2.3. Another aspect that is addressed is the contact to separation mode transition encountered upon the intersection of a hydraulically loaded crack with an in-situ crack. We propose an aperture-based approach to regularize the application of hydraulic load to newly loaded crack segments. The proposed dynamic contact conditions are incorporated in an interfacial damage model. A brief overview of the aSDG method and mesh adaptive operations needed for capturing complex fracture patterns is provided in §3. The contact / fracture model is used for the simulation of fracture under uniaxial compression and explosive loading and hydraulic fracturing / refracturing problems under different geometries and loading rates in §4.

2. Formulation

As will be further discussed in §3, we include inertia effects in the bulk by solving the elastodynamic equations. Contact and fracture can occur on interfaces that are either known a priori or are obtained as a part of solution. In this section we provide the formulation of an interfacial damage model that also incorporates dynamically consistent solutions for contact–stick and contact–slip modes. These solutions govern the solution on contact-fracture interfaces in rock. Cohesive models are commonly used to represent nonlinear material responses on a fracture surface. However, the enforcement of impenetrability condition and Coulomb friction relation is challenging for cohesive models. In lieu of a cohesive model, we represent the process of material degradation on a

fracture surface by an interfacial damage parameter D that ranges from zero for a fully bonded interface to $D = 1$ for a fully debonded one. There are two key components to the damage model. First, given the traction and velocity states on the two sides of an interface, dynamically consistent solutions for various contact modes are obtained by the solution of local Riemann problems in §2.1. Second as described in §2.2, by determining which mode(s) are active on a given point on a contact/fracture interface, we linearly combine the aforementioned Riemann solutions to derive macroscopic traction and velocity solutions. These macroscopic target solutions replace the *traction separation relation* (TSR) that is used in the context of cohesive models by specifying the traction (and velocity) state of the interface based on the traces of the solution from the opposite sides of the interface. Finally, in §2.3 we describe the process to smoothly apply hydraulic pressure on newly connected fracture surfaces to hydraulically loaded and propagating fracture network. Contact/separation model transitions in hydraulic fracturing are also described in §2.3.

2.1. Riemann solutions for different contact modes

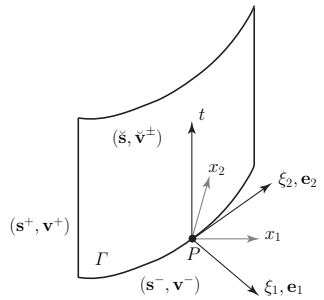

Figure 1: Local coordinate frame at arbitrary spacetime location P on a spacetime fracture surface Γ for a problem in two spatial dimensions.

For completeness, this section provides a short overview of different Riemann contact solutions from [37] with an improved and modified notation. Bonded, contact–stick, contact–slip, and separation are collectively called contact modes. The solutions for individual contact modes are obtained by solving local Riemann problems at a contact interface. A local coordinate frame at an arbitrary spacetime location P on contact interface Γ is illustrated in fig. 1. The local coordinates are (ξ_1, ξ_2, t), and the frame is oriented such that the ξ_1-direction aligns with the spatial normal vector on Γ from + to − sides. The quantities from the opposite sides of Γ, which are decorated with superscripts + and −, define the initial data for the Riemann problem. Distinct velocity traces, $\mathbf{v}^{\pm}$, and tractions, $\mathbf{s}^{\pm}$, from the traces of solution fields from the two sides. Tractions are defined by $\mathbf{s} = \boldsymbol{\sigma} \cdot \mathbf{n}$ in which the same spatial normal vector, $\mathbf{n}$, is used to compute $\mathbf{s}^+$ and $\mathbf{s}^-$ from the stress tensor $\boldsymbol{\sigma}$. The Riemann values at a given point P on the interface include components of the traction vector acting on the

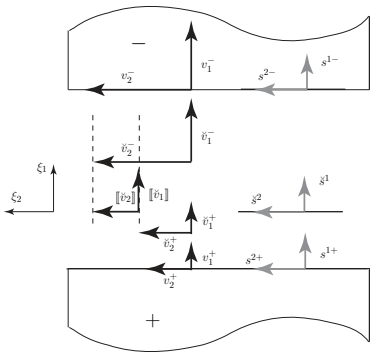

Figure 2: Top zoomed view of the point P from fig. 1. While the target traction solutions are the same $\breve{\mathbf{s}}^+ = \breve{\mathbf{s}}^- := \breve{\mathbf{s}}$, depending on a given contact mode kinematic compatibility, normal and tangential components of target velocities, $\breve{\mathbf{v}}^+$ and $\breve{\mathbf{v}}^-$, can be distinct from the two sides.

interface and traces of the velocity components from each side of the interface. We denote these by $(\breve{\mathbf{s}}, \breve{\mathbf{v}}^{\pm})$, as shown in the figure. Balance of linear momentum requires equality between the traction vectors obtained from the stress fields on opposite sides of the interface. That is, $\breve{\mathbf{s}}^+ = \breve{\mathbf{s}}^- := \breve{\mathbf{s}}$.

The kinematic compatibility conditions on the interface depend on whether the material interface is intact (perfectly bonded), or in the debonded case, on the specific contact mode. The target velocities on Γ are equal for bonded and contact–stick cases. For contact–slip case, while the impenetrability condition implies the continuity of target velocities in normal direction, $\breve{v}_1^+ = \breve{v}_1^-$, the tangential components can be discontinuous due to the slip condition. Finally, in separation model, all components of $\breve{\mathbf{v}}^+$ and $\breve{\mathbf{v}}^-$ can be discontinuous. Figure 2 shows a top and zoomed view of the point P in fig. 1. Interior traces of the solution are shown on the two sides of the interface and target values between the two sides. As evident, unlike target tractions, target velocities can be discontinuous and $[\![\breve{\mathbf{v}}]\!]$ denotes the corresponding jump.

The Riemann solutions are obtained by preserving the characteristic values of the elastodynamic problem and enforcing kinematic conditions pertinent to a given contact mode. For an isotropic material in linear elastodynamics, the spacetime characteristic trajectories in all directions are determined by the dilatational and shear wave speeds, $c_d^{\pm}$ and $c_s^{\pm}$,

$$c_{\mathrm{d}} = \sqrt{\frac{\lambda + 2\mu}{\rho}}, \qquad c_{\mathrm{s}} = \sqrt{\frac{\mu}{\rho}}. \tag{1}$$

where ρ is the mass density and λ, μ are the Lamé parameters.

The definition of characteristic values, [37], uses the impedance values given by,

$$Z^{i\pm} := \begin{cases} (c_d \rho)^{\pm} & i = 1 \\ (c_s \rho)^{\pm} & i = 2, 3 \end{cases} \tag{2}$$

in which the index i corresponds to spatial directions in the local frame shown in fig. 1.

After the solution of the local Riemann, the target values for contact–stick and bonded modes decorated with ST and B respectively, are obtained as,

$$\breve{s}^i_{\mathrm{B}} = \breve{s}^i_{\mathrm{ST}} = \breve{s}^i = \frac{s^{i+}Z^{i-} + s^{i-}Z^{i+}}{Z^{i-} + Z^{i+}} + \frac{Z^{i-}Z^{i+}}{Z^{i-} + Z^{i+}}(v_i^+ - v_i^-) \tag{3a}$$

$$\breve{v}_{\mathrm{B}_i} = \breve{v}_{\mathrm{ST}_i} = \breve{v}_i = \frac{s^{i-} - s^{i+}}{Z^{i-} + Z^{i+}} + \frac{v_i^+ Z^{i+} + v_i^- Z^{i-}}{Z^{i-} + Z^{i+}} \tag{3b}$$

the index i ranges from 1 to d the spatial dimension of the problem. No summation convention is implied for the repeated index i. The quantities $(s^{i+},\, v_i^+)$ and $(s^{i-},\, v_i^-)$ are shown in fig. 2 for a 2D ($d = 2$) geometry. As expected from (3b), we have $\breve{\mathbf{v}}^+ = \breve{\mathbf{v}}^- := \breve{\mathbf{v}}$.

In separation mode, $\breve{\mathbf{v}}^+$ and $\breve{\mathbf{v}}^-$ are fully independent. The Riemann tractions are, however, set equal to $\mathbf{S}$, the tractions specified by a particular fracture model or crack-surface loading. In §2.3.2, we discuss in detail how hydraulic pressure is incorporated in the target value $\mathbf{S}$. The Riemann solutions for the separation case, decorated by S, are then obtained by preserving the characteristic values on each side of the interface,

$$\breve{s}^i_{\mathrm{S}} = \breve{s}^i = S^i \tag{4a}$$

$$\breve{v}^{\pm}_{\mathrm{S}_i} = \breve{v}^{\pm}_i = v_i^{\pm} \pm \frac{S^i - s^{i\pm}}{Z^{i\pm}} \tag{4b}$$

Finally, the solutions for contact–slip mode are obtained by enforcing continuity of normal component of target velocity ($[\![\breve{v}]\!]_1 = 0$). This results in the same solutions for normal direction to that presented in (3). For the tangential directions, target tangential traction components are obtained from Coulomb friction law, resulting in possibly distinct components for tangential velocity target values ($[\![\breve{v}]\!]_i \neq 0,\ i = 2, 3$). The solution for tangential directions resemble those for separation mode in (4), with some technical details on how the direction of Coulomb friction is determined. The reader is referred to [37] for detailed derivation and expression for all the Riemann solutions.

2.2. Macroscopic target values and mode regularizations

2.2.1. Macroscopic target values

At any given point at the contact interface Γ the damage parameter D interpolates between *bonded* and *debonded* target solutions,

$$\mathbf{s}^* := (1 - D)\breve{\mathbf{s}}_B + D\breve{\mathbf{s}}_D \tag{5a}$$

$$\mathbf{v}^{*\pm} := (1 - D)\breve{\mathbf{v}}_B + D\breve{\mathbf{v}}^{\pm}_D \tag{5b}$$

where subscripts B and D indicate Riemann values for bonded (*cf.* (3)) and debonded conditions. Note that $\breve{\mathbf{v}}_B$ in (5b) is not decorated with side $\pm$ since from kinematic compatibility condition, same target value is enforced on both

sides as evident from (3b). The solution for the debonded part, itself is first divided into contact and separation modes. The relative part of contact to entire debonded $(1-D)$ fraction, is denoted by η. Finally, the contact mode can take either the contact–stick or contact–slip modes. The number γ denotes the ratio of contact–stick to entire contact fraction. Since the Riemann solutions for bonded and contact–stick modes are the same, *cf.* (3)), there are only the three distinct modes of bonded (B), contact–slip (SL), and separation modes (S). Thus, considering different contact modes within the debonded $(1-D)$ fraction, the solution (5) can be written as,

$$\mathbf{s}^* := a_{\mathrm{B}}\breve{\mathbf{s}}_{\mathrm{B}} + a_{\mathrm{SL}}\breve{\mathbf{s}}_{\mathrm{SL}} + a_{\mathrm{S}}\breve{\mathbf{s}}_{\mathrm{S}} \tag{6a}$$

$$\mathbf{v}^{*\pm} := a_{\mathrm{B}}\breve{\mathbf{v}}_{\mathrm{B}} + a_{\mathrm{SL}}\breve{\mathbf{v}}^{\pm}_{\mathrm{SL}} + a_{\mathrm{S}}\breve{\mathbf{v}}^{\pm}_{\mathrm{S}} \tag{6b}$$

where

$$a_{\mathrm{B}} = 1 - D + D\eta\gamma \tag{7a}$$

$$a_{\mathrm{SL}} = D\eta(1-\gamma) \tag{7b}$$

$$a_{\mathrm{S}} = D(1-\eta) \tag{7c}$$

again in (6b) $\breve{\mathbf{v}}_{\mathrm{B}}$ is not decorated with side notations $\pm$ since from (3b) the stick velocities are the same for both sides.

Equations (3), (4) provide target values for contact–stick / bonded and separation modes and the target values for contact–slip are provided in [37]. Once the values of D, η and γ are determined, macroscopic traction and velocity vectors are fully determined from (6) and (7). The determination of D, η and γ is discussed in the next three subsections.

2.2.2. Damage evolution law to determine D

At the top level of hierarchy of relative area fractions, the value of D must be determined. Here we adopt the rate-dependent interfacial damage model of [38] where damage rate is given by the evolution law,

$$\dot{D} = \begin{cases} \frac{1}{\tilde{\tau}}[1 - H(\langle D_t - D\rangle_+)] & D < 1 \\ 0 & D = 1 \end{cases}, \tag{8}$$

where $\tilde{\tau}$ is the *relaxation time*, and D_t is the *target damage value*. The function H takes the value of unity at zero and monotonically decreases to 0 at infinity. Following [39, 40], the particular form of H used in this work is given as $H(x) = \exp(-ax)$. It is evident from (8) that under monotonically increasing quasi-static loading, *i.e.,* when the load increases much slower than $\tilde{\tau}$, $\langle D_t - D\rangle_+ \to 0$ and $D \to D_t$. That is, D_t is the damage value for the present interface condition, if the loading had been applied under quasi-static condition. The positive part operator in $\langle D_t - D\rangle_+$ ensures that D is a nondecreasing function of time.

We assume D_t to be a function of bonded Riemann traction (3a) through

the value of *effective stress* [1] $\breve{s}$,

$$\breve{s} := \sqrt{\langle \breve{s}_{\mathrm{B}}^1 \rangle_+^2 + (\beta \breve{\tau}_{\mathrm{B}})^2} \tag{9}$$

where $\breve{s}_{\mathrm{B}}^1$ and $\breve{\tau}_{\mathrm{B}} := \sqrt{\sum_{j=2}^{d} \left(\breve{s}_{\mathrm{B}}^j\right)^2}$ refer to the normal component and the magnitude of the tangential component of bonded Riemann traction. The *shear stress factor*, β, controls mode mixity. This definition of effective stress is common in fracture mechanics and is adopted from [41]. Finally, D_t is expressed as,

$$D_t = \begin{cases} 0 & \breve{s} < \underline{s}, \\ \frac{\breve{s}-\underline{s}}{\bar{s}-\underline{s}} & \underline{s} \le \breve{s} < \bar{s}\ , \\ 1 & \bar{s} \le \breve{s} \end{cases} \tag{10}$$

where $\underline{s}$ and $\bar{s}$ denote, respectively, effective traction thresholds for the onset of additional damage evolution and for the attainment of maximum damage rate. We refer to $\bar{s}$ as the *fracture strength*.

A few points should be clarified regarding the definition of $\breve{s}$. First, based on the form of $\breve{s}$ and damage evolution (8), $\bar{s}$ corresponds to the quasi-static tensile strength. The maximum attainable tensile strength increases under higher loading rates, due to the rate form of the damage evolution law. Second, quasi-static shear strength is equal to $\breve{s}/\beta$. Third, the use of bonded Riemann tractions rather than the macroscopic traction vector $\mathbf{s}^*$ from (6a) in the definition of effective stress is not only physically justified (as damage evolution is driven by the strength of impinging waves), but also prevents premature termination of damage evolution; if $\mathbf{s}^*$ had been used since its value decreases as $D \to 0$, from (10) $\breve{s}$ eventually falls below $\underline{s}$, thus preventing the full debonding of an interface.

2.2.3. Determination and regularization of η

The determination and analysis of η is one of the main emphasis of this paper. In [37], this analysis was provided for $S^1 = 0$ in (4a). However, it does not carry over to hydraulic fracturing and in general to problems where $S^1 \neq 0$. The details of the newly proposed approach are provided below.

Figure (3) shows the 2D phase space for analytical η in terms of nondimensional normal separation velocity jump $[\![\breve{v}_{\mathrm{S}_1}]\!]/\tilde{v}$ and normal displacement jump $\delta' := \delta/\tilde{\delta}$. The fracture scales $\tilde{v}, \tilde{s}, \tilde{\delta}$ are described later. Let u_1^- and u_1^+ be the normal component of displacements from $-$ and $+$ sides. It is clear that the interface is in separation mode ($\eta = 0$) if the normal displacement jump $\delta := u_1^- - u_1^+$ is positive. Moreover, $\delta < 0$ is unacceptable as inter-penetration

[1] The effective stress refers to a scalar stress measure that drives damage evolution and should not be confused with its use in rock mechanics referring to the compressive part of the normal traction minus the pore pressure.

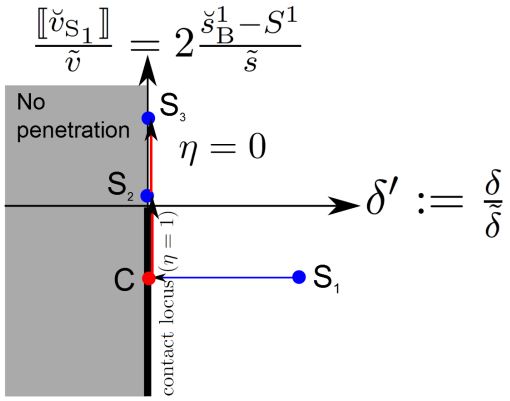

Figure 3: Maps of separation ($\eta = 0$) and contact ($\eta = 1$) modes based on normal separation velocity jump $[\![\breve{v}_{S_1}]\!]$ and normal displacement jump δ. The separation-to-contact (S_1 to C) and contact-to-separation (C to S_2 or S_3) transitions are discussed in §2.2.3.

is not permitted. For $\delta = 0$ the choice on whether contact or separation mode holds depends on the velocity at which the two sides of interface hypothetically separate. To clarify this, among the three modes of bonded (B), contact–slip (SL), and separation (S), it is only the latter that can have nonzero normal displacement jump. Thus, from (6) and (7c) we have,

$$[\![v_1^*]\!] = v_1^{*-} - v_1^{*+} = a_S [\![\breve{v}_1]\!] = D(1-\eta)[\![\breve{v}_{S_1}]\!] \tag{11}$$

where $[\![\breve{v}_{S_1}]\!] = \breve{v}^-_{S_1} - \breve{v}^+_{S_1}$. Clearly, the value of η has an influence only if $D > 0$, otherwise the interface is fully in bonded mode and as expected from either (5) or (6) $\mathbf{s}^* := \breve{\mathbf{s}}_B$, $\mathbf{v}^* := \breve{\mathbf{v}}_B$. Thus, to determine the value of η when $\delta = 0$ we assume $D > 0$ in (11). If $[\![\breve{v}_{S_1}]\!] < 0$, then we must have $\eta = 1$; otherwise $[\![v_1^*]\!] < 0$ which is not permissible as it implies interpenetration given that δ is assumed to be zero. On the other hand, if $[\![\breve{v}_{S_1}]\!] > 0$ from the two choices of $\eta = 0$ and $\eta = 1$, the condition $\eta = 0$ is the physical choice, since it is a positive $[\![\breve{v}_{S_1}]\!]$ that can take an interface already at contact mode ($\delta = 0$, $[\![\breve{v}_{S_1}]\!] < 0$) back to separation mode. Thus, for $\delta = 0$, the sign of $[\![\breve{v}_{S_1}]\!]$ determines η, as shown in (3).

Next, we relate $[\![\breve{v}_{S_1}]\!]$ to traction quantities which are generally easier to compute, particularly in hydraulic fracturing application. By plugging the values $\breve{v}^\pm_{S_1}$ from (4b) in $[\![\breve{v}_{S_1}]\!] = \breve{v}^-_{S_1} - \breve{v}^+_{S_1}$ and using the identity (3a) we obtain,

$$\tilde{Z}^1 [\![\breve{v}_{S_1}]\!] = 2(\breve{s}^1_B - S^1) \quad \Rightarrow \tag{12a}$$

$$\tilde{Z}^1 [\![v_1^*]\!] = 2D(1-\eta)(\breve{s}^1_B - S^1) \tag{12b}$$

where

$$\tilde{Z}^1 := \frac{2Z^{1-}Z^{1+}}{Z^{1-} + Z^{1+}} \tag{13}$$

is defined as the impedance of the interface for normal waves. It should be noted that in [37], $\breve{s}^1_{\mathrm{B}}$, rather than $[\![\breve{v}_{\mathrm{S}_1}]\!]$ is used on the vertical axis of the phase space in fig. 3. From the form of (12a), it is evident that the former approach is correct only if $S^1 = 0$.

Finally, the quantities in the axes of fig. 3 are normalized by their corresponding fracture scales. This facilitates choosing nondimensional parameters that are used in the regularized version of η, described shortly after. In [42, 43] fracture scales are derived for a general cohesive model. The same analysis can be extended to the damage model with evolution equation (8) to obtain fracture displacement scale $\tilde{\delta}$ and velocity scale $\tilde{v}$,

$$\tilde{\delta} = \frac{\tilde{\tau}\tilde{s}}{\tilde{Z}^1} \tag{14a}$$

$$\tilde{v} = \frac{\tilde{\delta}}{\tilde{\tau}} = \frac{\tilde{s}}{\tilde{Z}^1} \tag{14b}$$

where the stress (strength) scale for the damage model is $\tilde{s} = \bar{s}$ based on the particular form of D_t in (10). Thus, equations (14), (12a), and (13) yield the form of normalized axes in fig. 3.

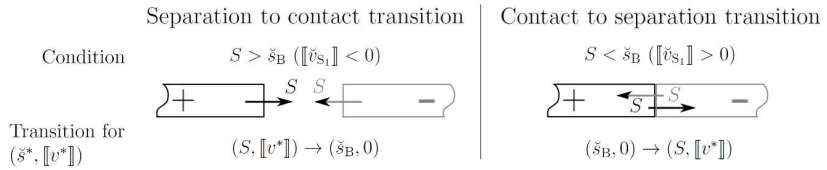

Figure 4: The schematic of contact separation transitions where the magnitude of characteristics distribute differently between normal traction $\breve{s}^*$ and normal velocity jump $[\![v^*]\!]$.

Contact separation mode transitions implied by fig. 3 can physically be nonsmooth in that tractions and velocities on either sides can suffer jumps upon such transitions. To simplify the following discussion, we temporarily assume $D = 1$, that is the interface is fully debonded. The same conclusions can be made for $D > 0$ and for $D = 0$ clearly there is no debonded mode to transition between the contact and separation modes. Figure 4 shows the schematics of these two transitions. The superscripts and subscripts 1 for normal traction and velocity components are removed for brevity.

For the separation-to-contact transition, we start from the separation mode; *i.e.,* the space of $\eta = 0$ in fig. 3. Given that a contact mode is supposed to occur, the separation velocity must be negative ($[\![v^*]\!] < 0$) so that the two sides can approach each other. This corresponds to the point S_1 approaching point C in fig. 3. From (12b) we observe that this is equivalent to $S > \breve{s}_{\mathrm{B}}$. Given that upon transition to contact mode, η changes from 0 to 1, $\breve{s}^*$ suddenly jumps from the separation mode traction S to its bonded target value $\breve{s}_{\mathrm{B}}$; *cf.* (3a), (4a) (6), (7), and note that $D = 1$. Similarly, the separation velocity $[\![\breve{v}_{\mathrm{S}_1}]\!]$ jumps from $2(\breve{s}_{\mathrm{B}} - S)/\tilde{Z}$ to zero. That is, the kinetic energy implied by relative motion of

the two sides of an interface is suddenly transferred (added) to strain energy. This jump is physical and causes the propagation of sharp waves inside $-$ and $+$ domains. Clearly, the larger $S - \check{s}_{\mathrm{B}}$, the larger the magnitude of these waves.

The contact-to-separation transition, takes a point similar to C in fig. 3 and moves it into separation mode by reaching a stage when $[\![\check{v}_{\mathrm{S}_1}]\!] \geq 0$. This path is shown by the red arrow $C \rightarrow S_2$ (or $C \rightarrow S_3$) in the figure. Similar to separation-to-contact transition $(\check{s}^*, [\![v^*]\!])$ suffer jump between contact and separation states; in this case $\check{s}^*$ changes from $\check{s}_{\mathrm{B}}$ to S while $[\![\check{v}_{\mathrm{S}_1}]\!]$ changes from negative $2(\check{s}_{\mathrm{B}} - S)/\tilde{Z}$ to its corresponding zero or positive values at S_2 or S_3, respectively. Now, what almost always makes this transition smooth is the way $[\![\check{v}_{\mathrm{S}_1}]\!]$ increases on a contact interface. Often, impinging characteristic waves gradually lose their compressive strength until $[\![\check{v}_{\mathrm{S}_1}]\!] \rightarrow 0^-$. This occurs by the approach of tensile (separation-inducing) finite width (non-sharp) waves from the sides of the interface. Thus, unlike the previous transition, contact-to-separation transition does not require a regularization in this case. The path of this transition is shown by C to S_2 in fig. 3 and right at the moment of transition $[\![\check{v}_{\mathrm{S}_1}]\!] = 0$, thus stress and separation velocity do not suffer jumps.

The previous contact-to-separation transition is often smooth and is typically driven by the change in $\check{s}_{\mathrm{B}}$ (through impinging waves from the bulk). However, $[\![\check{v}_{\mathrm{S}_1}]\!]$ can also become positive if S is sufficiently reduced (becomes more compressive). This is very relevant to hydraulic fracturing where upon the intersection of a hydraulically loaded crack and an in-situ crack, a hydraulic pressure $p_h = -S$ larger than the in-situ pressure $\sigma_h = -\check{s}_{\mathrm{B}}$ can suddenly cause a transition of C to S_3 in fig. 3. Clearly, this contact-to-separation transition is non-smooth.

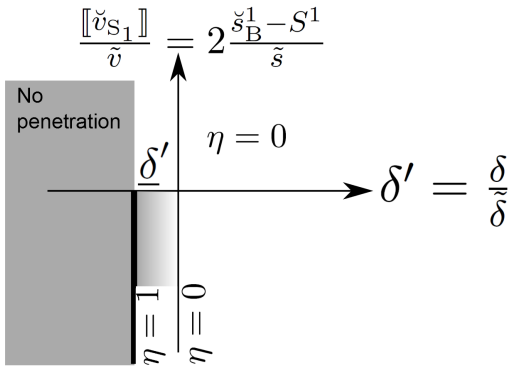

Figure 5: Map of regularized η based on normal separation velocity jump $[\![\check{v}_{\mathrm{S}_1}]\!]$ and normal displacement jump δ.

To summarize, separation-to-contact transition is physically non-smooth. In [37] a regularization approach based on δ' is proposed that smoothens this transition. This regularization even if not essential, greatly reduces computational costs in resolving sharp wave fronts generated by separation-to-contact transi-

tions. Figure 5 depicts a regularized version of fig. 3. The parameter $\underline{\delta}' < 0$ denotes the maximum nondimensional penetration permitted in the regularized model, corresponding to displacement jump $\underline{\delta}'\tilde{\delta}$. The particular form of the function that regularizes η from unity to zero for δ' from $-\underline{\delta}'$ to 0 and the exceptionally smooth contact-separation mode transition behavior of this model are described in [37]. Unlike cohesive models, this model possesses a maximum penetration which can also be numerically tuned without resulting in a stiff system of equations or nonconvergence issues.

As for the contact-to-separation transition, it typically does not require any regularization. Moreover, η should immediately turn to zero as soon as $[\![\breve{v}_{\mathrm{S}_1}]\!] \to 0^-$, otherwise contact-to-separation transition is artificially prevented or other nonphysical responses arise, see [37] for further discussion on this. On the other hand, for cases that C suddenly jumps to S_3, through the intersection of a hydraulically loaded and an in-situ crack, the transfer of the hydraulic load must be regularized such that the path from C to S^3 is smoothly taken from negative $[\![\breve{v}_{\mathrm{S}_1}]\!]$ values, past S_2, until the final stage S^3 is realized when the hydraulic pressure is fully applied on the surfaces of the in-situ crack. The gradual application of hydraulic pressure, upon intersection, not only smoothens contact-to-separation mode transition but also eliminates the nonphysical sudden loading of the entire length of the in-situ crack. This pressure regularization scheme is discussed in §2.3.2 and its impact is studied through the examples in §4.3.

2.2.4. Mohr-Coulomb friction model to determine γ

The binary value of $\gamma \in \{0, 1\}$ is determined based on the particular friction model employed. For example, for a linear Mohr-Coulomb friction model on a debonded interface we have $\gamma = 0$ when $|\breve{\tau}_{\mathrm{B}}| > k \left\langle -\breve{s}^1_{\mathrm{B}} \right\rangle_+$ and one otherwise, where k is the friction coefficient. Similar to separation-to-contact transitions, stick–slip mode transitions are reported to generate numerical artifacts. The apparent source of non-smoothness arises from the original form of Coulomb friction law where the direction of tangential traction is determined by the slip velocity; since the latter quantity vanishes at stick–slip transitions the direction of tangential traction becomes ambiguous. While numerical regularizations such as those in [44, 45, 46] are proposed to resolve this ambiguity and eliminate numerical artifacts at transition instances, in [37] we have shown that the transition is in fact physically smooth and the direction of tangential (slip) traction is always well-defined. As a result, the value of γ is not regularized herein; please see [37] for more details.

2.3. Application of hydraulic pressure

For accurate modeling of hydraulic fracturing, the fluid flow in fracture network should be coupled with the deformation of crack surfaces as in [47, 48]. Moreover, in studies such as [49, 50, 51] fluid flow in rock domain is also considered by solving poroelastic equations. However, for fracture analysis of shale gas reservoirs with low permeability the application of constant fluid pressure is an

acceptable approximation; see for example [52] and the references therein. For very tight formations, the poroelastic effects and the leak-off of fluid across crack faces can also be neglected. Besides, for low viscosity fracturing fluids such as treated water, the constant fluid pressure assumption is even more acceptable, especially near the wellbore. The accuracy of constant pressure approximation is demonstrated in [53, 54, 55, 56] for rocks with high fracture toughness and/or hydraulic fluids with low viscosity. In the remainder of this manuscript, we assume the hydraulic pressure p to be spatially constant, except through the pressure regularization scheme that modifies p near crack intersection sites, as described in this section.

2.3.1. Pressure factor

By using a simplicial complex representation of cracks and modeling their connectivity by a disjoint set data structure [57], the authors provide a means to transfer hydraulic pressure to an in-situ crack when a hydraulically loaded crack intersects it. This representation, however, only provides information whether a crack is hydraulically loaded or not, resulting in two potential problems. First, if a hydraulically-loaded crack intersects a long crack, clearly not all the points on that crack surface will immediately experience the hydraulic pressure exerted at the connection of the two cracks. Second, as described in §2.2.3 traction and velocity fields experience a sudden jump if the full hydraulic pressure is suddenly exerted on newly connected crack surfaces; the in-situ compressive stress between crack surfaces will suddenly jump to a potentially much greater hydraulic pressure if the hydraulic load is immediately transferred. We provide an aperture-based approach that regularizes the transfer of hydraulic load to newly connected crack surfaces and remedies both aforementioned problems.

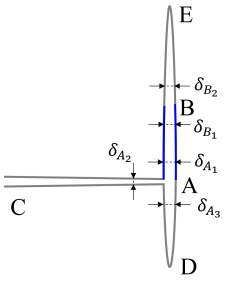

Figure 6: Regularization of the applied hydraulic pressure on a crack surface based on the apertures of connected crack segments.

Figure 6 shows the intersection of a hydraulically loaded crack, segment CA, with an in-situ or otherwise unloaded crack, *i.e.,* the extension of DE. The goal is to regularize the applied hydraulic pressure for the sample segment AB. Accordingly for an arbitrary point P, such as A and B, we define,

$$\delta_{P_{\max}} = \max_i \left(\delta_{P_i}\right) \tag{15}$$

where δ_{P_i} are the apertures of the hydraulically loaded and connected cracks to point P, as shown in the figure for points A and B. Then the *pressure factor* f_p or point P is defined as,

$$f_p(P) = \begin{cases} 0 & \delta'_P \leq 0 \\ \frac{\delta'_P}{\bar{\delta}'} & 0 < \delta'_P < \bar{\delta}' \\ 1 & \bar{\delta}' < \delta'_P \end{cases} \tag{16}$$

where $\delta'_P = \delta_{P_{\max}}/\tilde{\delta}$ is the maximum aperture at point P, normalized by the displacement scale $\tilde{\delta}$, *cf.* (14a). The nondimensional parameter $0 < \bar{\delta}' \ll 1$ basically regularizes the application of hydraulic load from $\delta_{P_{\max}} = 0$ to $\delta_{P_{\max}} = \bar{\delta}'\tilde{\delta}$. That is, the maximum aperture of connected hydraulically-loaded cracks smoothens the sudden transition of C to S_3 in fig. 3.

A few important aspects of the model are briefly commented on. First, the locations for which apertures are measured are not right at a given point. For example, as shown in fig. 6 for points A and B, there is an offset behind the point of consideration on a given crack surface. Second, the pressure factor on a crack surface is linearly interpolated based on the values at the end vertices, for example points A and B in fig. 6. Third, to ensure that the regularization is not influenced by the level of mesh adaptivity, and in general element sizes, the offset is set to be a fraction of a fracture related length scale, *e.g.,* fracture process zone size (*cf.* equation (29f) in [42]). Fourth, the objective of the regularization is to activate and smoothen the sudden application of hydraulic load upon the intersection of two cracks. While in this work spatially constant hydraulic pressure is applied on on crack surfaces, the same regularization scheme can be applied to regularize the onset of the application of hydraulic pressure based on other models such as lubrication equation. The condition $\bar{\delta}' \ll 1$ ensures that the pressure regularization is only active for the very early stages of crack opening.

2.3.2. Regularized hydraulic pressure

It is evident from (16) that f_p for a point P tends to one when maximum aperture $\delta_{P_{\max}}$ reaches the threshold value of $\bar{\delta}'\tilde{\delta}$. Pressure factor f_p basically specifies the fraction of hydraulic pressure that is enforced. For the remaining fraction, $1 - f_p$, a target normal traction that would have been active in the absence of hydraulic pressure should be enforced. Accordingly, the normal component of target separation traction, *cf.* (4a) is given by,

$$S^1 = -\left\{ f_p p_h + (1 - f_p)\langle -\breve{s}^1_{\mathrm{B}} \rangle_+ \right\} \tag{17}$$

where p_h is the hydraulic pressure at the given space and time position. The second term in the interpolation $\langle -\breve{s}^1_{\mathrm{B}} \rangle_+$ is the compressive traction under bonded (contact) mode. Given that S is one of the three contact modes within debonded part (D fraction) of damage model, *cf.* §2.2.1 and (6a), (5a), the $(1 - f_p)$ part in (17) cannot withstand any tensile traction. The positive part in $\langle -\breve{s}^1_{\mathrm{B}} \rangle_+$ ensures that zero compressive stress in considered when the bonded normal traction is

tensile ($\breve{s}^1_{\mathrm{B}} > 0$). The front minus sign in (17) is needed to express the regularized compressive traction with tensile positive convention. Finally, in the present work $S^2 = 0$, as it is assumed that no shear traction is applied on crack surfaces through the fluid's viscous effects. If needed, the shear traction can also be regularized using f_p.

Lastly, we want to investigate under what conditions, the hydraulic pressure p_h is large enough to cause crack opening. When the interface is in (partial) contact condition, which implies $\underline{\delta}' \leq \delta \leq 0$, it transitions to separation mode if and only if $[\![\breve{v}_{\mathrm{S}_1}]\!] \geq 0$, as discussed in §2.2.3. By plugging the pressure factor regularized form of S^1 from (17) into (12a) we observe,

$$\tilde{Z}^1 [\![\breve{v}_{\mathrm{S}_1}]\!] = 2 \left\{ f_p \left(p_h + \breve{s}^1_{\mathrm{B}} \right) + (1 - f_p) \langle \breve{s}^1_{\mathrm{B}} \rangle_+ \right\} \tag{18}$$

Since $p_h \geq 0$, it is evident that $[\![\breve{v}_{\mathrm{S}_1}]\!] \geq 0$ if the normal bonded traction is tensile, that is $\breve{s}^1_{\mathrm{B}} \geq 0$. This corresponds to a case where the impinging characteristics on the crack surface tend to open the crack. Clearly, the crack surface pressure accelerates the speed at which the crack surfaces separate. The more interesting case is when impinging characteristics attempt to close the crack surface ($\breve{s}^1_{\mathrm{B}} < 0$), *e.g.,* when the crack is under in-situ compressive stresses. Under this condition,

$$\tilde{Z}^1 [\![\breve{v}_{\mathrm{S}_1}]\!] = 2 f_p \left(p_h + \breve{s}^1_{\mathrm{B}} \right) \quad \text{when } \breve{s}^1_{\mathrm{B}} < 0 \tag{19}$$

Thus, independent of the sign of $\breve{s}^1_{\mathrm{B}}$ we obtain,

$$[\![\breve{v}_{\mathrm{S}_1}]\!] \geq 0 \text{ (and } [\![\breve{v}_1]\!] \geq 0) \quad \Leftrightarrow \quad p_h \geq -\breve{s}^1_{\mathrm{B}} \tag{20}$$

Accordingly, when a crack with zero normal separation ($\delta = 0$) is hydraulically loaded, it transitions to separation mode if and only if the hydraulic pressure is greater than bonded pressure $-\breve{s}^1_{\mathrm{B}}$, *cf.* fig. 5. That is, hydraulic pressure must be greater than the ambient pressure (whose value is given by $-\breve{s}^1_{\mathrm{B}}$) to open the crack. Since $\tilde{Z}^1 [\![\breve{v}_1]\!] = 2 f_p D (1 - \eta) \left(p_h + \breve{s}^1_{\mathrm{B}} \right)$ (for $\breve{s}^1_{\mathrm{B}} < 0$), *cf.* (11), we observe that speed at which crack faces separate is linearly proportional to f_p with $[\![\breve{v}_1]\!]$ being zero at initial stages of application of hydraulic load and reaching its maximum when f_p reaches one. This in essence is the effect of pressure regularization that smoothens the application of hydraulic load and regularizes the transition of C to S_3 in fig. 3. In fact, if in (17) the $(1 - f_p)$ part was not included, *i.e.,* if hydraulic pressure were gradually regularized to its pick value without starting from the ambient stress field, many of the aforementioned properties would be lost and the regularization could be rendered ineffective.

3. Implementation

This section provides a short overview of the *asynchronous spacetime Discontinuous Galerkin* (aSDG) method that is needed for the interpretation of results in §4. In the bulk we solve the elastodynamic equation of motion, $\nabla \cdot \boldsymbol{\sigma} + \rho \mathbf{b} = \rho \dot{\mathbf{v}}$,

where $\boldsymbol{\sigma}$ is the stress tensor, $\mathbf{b}$ is the body force vector, and $\mathbf{v}$ is velocity. We use the aSDG method [58] to solve the elastodynamic problem. For 2D problems considered herein, we start from a triangulation that represents the spatial domain at initial time. Figure 7 shows how the aSDG method advances the solution in time, by each time *pitching* a vertex in time to form a *patch*, *i.e.,* a group, of spacetime tetrahedral elements that are solved simultaneously. For example, in fig. 7(a) the patch of elements shown in the right is already solved, whereas the left patch is just pitched. If the solution of all the elements in a patch is acceptable, the patch is accepted and the elements are added to the spacetime mesh. As shown, at each stage of solution a new patch is erected and solved. This process continues until the entire spacetime domain is filled with spacetime elements.

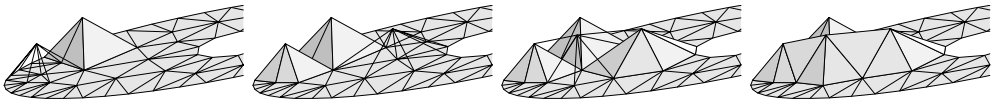

Figure 7: Tent-Pitcher in $2D\times$time; the time-axis is vertical. Wireframe renderings depict new patches of tetrahedra to be solved. Patches with opaque surfaces are already solved (reproduced from [58]).

At each instant, the collection of triangular *outflow* faces of the farthest elements in time is called the *front mesh*. As can be seen in fig. 7, the front mesh is asynchronous as vertices can have different advances in time. The height at which a vertex can be pitched in time is limited to an extent that keeps all the outflow faces of the elements in that patch *causal*, in that elastodynamic waves only exit these facets in spacetime. While this aspect is similar to *explicit* time marching method, the aSDG method is fully asynchronous and unlike explicit schemes very small elements do not pose small time advances for the entire space mesh. Moreover, the solution within a patch is implicit. Finally, given that at each instant only a patch of a few elements (rather than the entire spatial domain) is solved, the solution cost scales linearly versus the number of elements; see [59] for more details on the *Tent-Pitcher* algorithm.

Mesh adaptivity in spacetime is used for two purposes in the aSDG method. Figure 8 shows a spatial view of a sample patch, which can hypothetically correspond to the top view of any of the patches shown in fig. 7. The angular distribution of effective stress $\breve{s}$, *cf.* (9), around the top vertex V is shown by radial distance to it. A crack will be nucleated at V if the effective stress at any given angle θ exceeds the strength threshold $\underline{s}$ (see (10)) at V. The propagation direction is then decided at angle(s) with local maximum $\breve{s}$. For example, in fig. 8 a crack will propagate from V along the line VP. If this direction is not aligned with existing inter-element boundaries in that patch, mesh adaptive operations create a new element boundary along this direction by either realigning the closest element boundary or refining the front element containing it. The same approach is used for crack propagation from an already existing crack tip at vertex V; see [61] for the details of this crack tracking scheme applied to rock fracture.

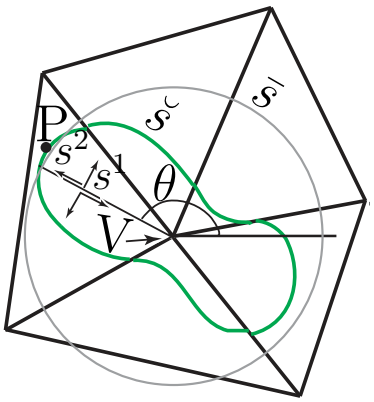

Figure 8: The angular distribution of effective stress $\breve{s}$ and fracture strength threshold $\underline{s}$ around vertex V at the top of a patch. The magnitude of these parameters for a given angle θ is mapped to radial distance from V. (reproduced from [60]).

The second set of adaptive operations are used to improve solution accuracy and efficiency. For example, if energy dissipation in any of the elements in the left patch of fig. 7(a) is larger than a user-specified tolerance, that patch is rejected and the triangles at the base of this patch are refined. The next time Tent Pitcher resumes in that region, smaller elements in space and time are generated. Finite element refinement and coarsening algorithms and geometric meshing details of this scheme are provided in [36]. Finally, on contact and fracture surfaces we use a secondary error indicator that ensures contact and fracture constitutive equations are solved accurately. The dual control of bulk energy dissipation and contact / fracture face errors is described in [62]. In summary, the asynchronous and local solution features of the aSDG method, exact capturing of crack propagation direction, and control of bulk and fracture errors results in a highly accurate and efficient solution scheme to model rock fracture.

4. Numerical examples

In the first example, presented in §4.1, the failure of a rectangular domain under uniaxial compressive load is studied. The three examples presented in §4.2 study the nucleation and propagation of cracks under highly dynamic explosive loads exerted on the wellbore wall. One key aspect of both problems is the lack of macroscopic stress concentration points. The stochastic fracture strength model from [60] is employed to enable nucleation of cracks from the weakest points and prevent nonphysically sudden and spatially global fracture of the rock mass.

The second group of results pertain to problems where cracks grow from hydraulically loaded perforations around a wellbore. The existence of initial macroscopic stress concentration points, *i.e.,* crack tips, and nonzero hydraulic

pressure are the main differences of these problems compared to those in §4.1 and §4.2. In the two examples presented in §4.3 we demonstrate the need to regularize the application of hydraulic pressure, especially when a hydraulically loaded crack intersects an unloaded crack. The re-fracture example in §4.4 demonstrates that the regularization scheme in §2.2.3 can smoothly model transition between contact and separation modes. Finally, the numerical examples in §4.5 are provided to study the effect of loading rate in a refracture problem and to study the interaction of hydraulically loaded cracks with in-situ microcracks. Except for the problem in §4.1, rock is under confining pressure of 2.425 MPa in all directions at the initial time and its material properties are: Young's modulus $E = 20$ GPa, mass density $\rho = 2500$ kg/m^3, and Poisson's ratio $\nu = 0.20$. The interface properties are: fracture strength $\bar{s} = 2$ MPa and relaxation time $\tilde{\tau} = 30$ ms.

4.1. Dynamic fracture under uniaxial compressive loading

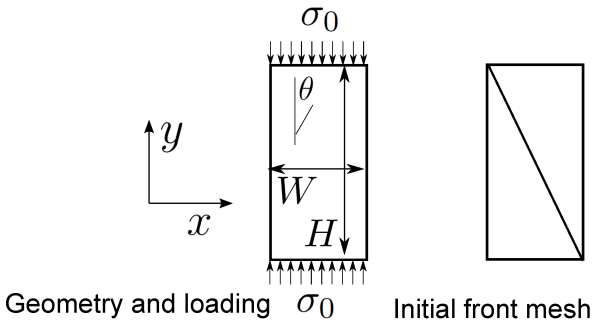

Figure 9: Problem description for the rectangular-domain under dynamic uniaxial compressive load.

The geometry, boundary condition, and initial front mesh for a rectangular domain, $W = 0.08$ m and $H = 0.16$ m, subject to uniaxial compressive dynamic load σ_0 is shown in fig. 9. The load σ_0 ramps from zero to a sustained value of 2.5MPa in 10 microseconds. The material properties are: Young's modulus $E = 65$ GPa, mass density $\rho = 2600$ kg/m^3, and Poisson's ratio $\nu = 0.27$. The interface properties are: mean fracture strength $\mathbb{E}(\bar{s}) = 4.5$ MPa, relaxation time $\tilde{\tau} = 30$ ms, and friction coefficient $k = 0.3$.

The goal of this example is to demonstrate the nucleation and propagation of cracks in a domain without explicit representation of initial flaws, and propagation of nucleated cracks in mode *II*, *i.e.,* due to the activation of slip mode along their faces. As will be discussed below, under uniaxial compressive loading and using the effective stress model (9), cracks nucleate at the angle $\theta = 45°$; *cf.* fig. 9 as the stress waves travel inward. When a homogeneous material model is employed, cracks are expected to nucleate at all points on the wave fronts. However, this clearly is not physical and cracks will only nucleate from weakest

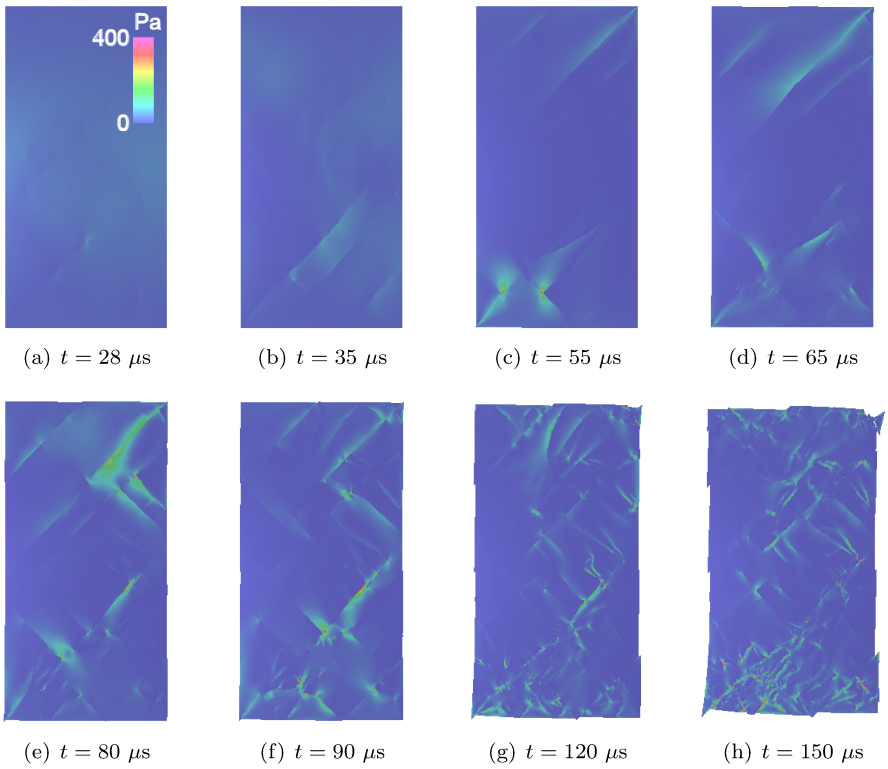

(a) $t = 28\ \mu$s (b) $t = 35\ \mu$s (c) $t = 55\ \mu$s (d) $t = 65\ \mu$s

(e) $t = 80\ \mu$s (f) $t = 90\ \mu$s (g) $t = 120\ \mu$s (h) $t = 150\ \mu$s

Figure 10: Strain-energy density map for the rock domain under uniaxial compressive load.

points in rock. Various approaches are used in the literature to incorporate some inhomogeneity in rock properties to address this issue in modeling uniaxial compressive failure; see for example [63, 2, 1, 3]. To represent rock inhomogeneity, it is assumed that its fracture strength follows a Weibull model, conceptually similar to the approach used in [1]. For the Weibull parameters used the standard deviation of fracture strength is $\varsigma(\bar{s}) = 956$kPa. For the details of the statistical nucleation model based on Weibull distribution, the reader is referred to [60].

Before the nucleation of any cracks, x and y are the principal axes for the stress tensor for all points in the domain with zero and negative values for σ_{xx} and σ_{yy}, respectively. Thus, on any potential crack surface with angle θ, *cf.* fig. 9, the normal stress is compressive and the effective stress from (9) reduces to the shear stress on that plane. Since, the shear stress is maximum on planes of angle $\pm 45°$, cracks are expected to form and propagate on these planes in mode *II*.

To verify this prediction, we refer to figs. 10 and 11 for a sequence of solution visualization. The strain energy density is $U := \frac{1}{2}\boldsymbol{\sigma} : \boldsymbol{\epsilon}$, where $\boldsymbol{\epsilon}$ is the strain tensor. In fig. 10 and all subsequent solution visualization U is mapped to color field, where zero to maximum values are mapped to blue-to-purple color range.

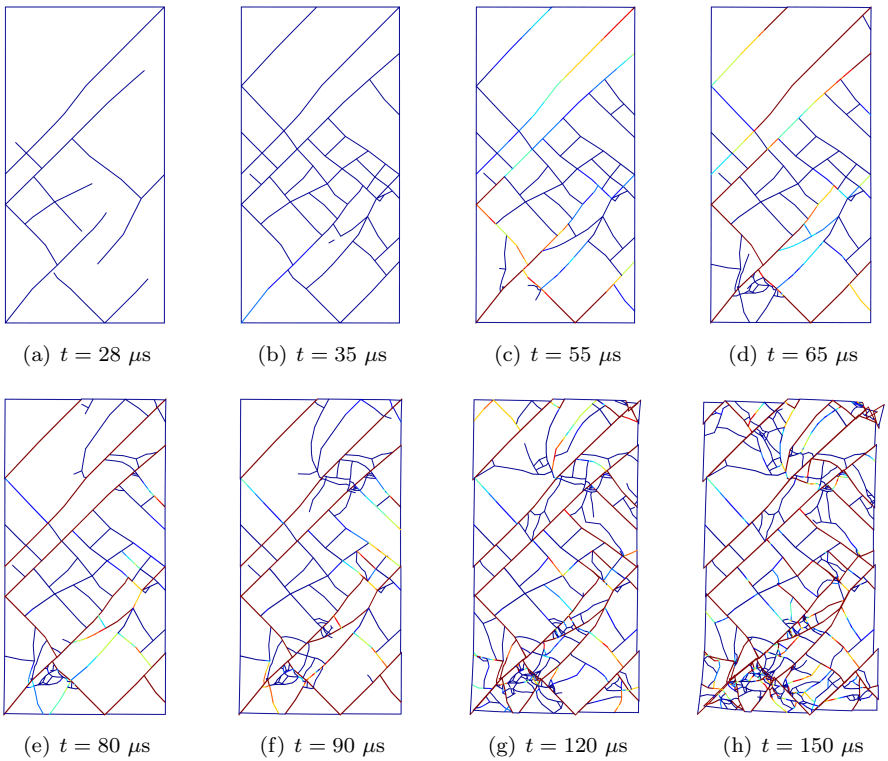

(a) $t = 28\ \mu$s (b) $t = 35\ \mu$s (c) $t = 55\ \mu$s (d) $t = 65\ \mu$s

(e) $t = 80\ \mu$s (f) $t = 90\ \mu$s (g) $t = 120\ \mu$s (h) $t = 150\ \mu$s

Figure 11: Deformed shape and fracture pattern for the rock domain under uniaxial compressive load. Damage on crack segments in the range, $D \in [0,\ 1]$, is mapped to a blue-to-red color range.

The unit of U is $\mathrm{J/m^3} = \mathrm{Pa}$. In fig. 11, only crack segments are shown on the deformed geometry. The color on crack segments demonstrate the local damage level. This figure is better to observe the evolution of fracture pattern.

Figures 10(a) and 11(a) show a 45 degree crack propagating from the lower left corner. In fig. 10(b) and fig. 11(b), this crack has propagated further and a few other cracks have propagated at angles close to $\pm 45°$. While, the location of the cracks are determined by sampling the weakest fracture strengths at the vertices on the front mesh, *cf.* §3, their propagation direction is very close to the predicted $\pm 45°$ angles. In figs. 10(c) to 10(f) (figs. 11(c) to 11(f)) it is observed that the points of stress concentration and the corresponding active mode *II* crack slip regions change. This is due to the scattering of the waves from the domain boundaries and crack surfaces. Finally, at later stages shown in fig. 10(g) and fig. 10(h) (fig. 11(g) and fig. 11(h)), finer fragmented clusters are formed and several slip systems with larger displacements are observed.

Due to complex wave scattering events and the interaction of cracks, various transitions between contact–stick, contact–slip, and even slight separation are

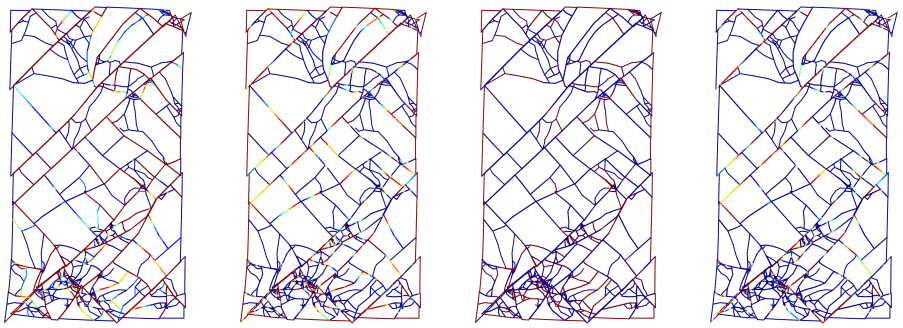

(a) D (b) η (c) γ (d) a_{SL}

Figure 12: Contact and fracture fractions for the rock domain under uniaxial compressive load at $t = 150$ μs. The corresponding values, in the range of $[0,\ 1]$ are mapped to a blue-to-red color range.

encountered in this problem. Consequently, the spatial location of active slip regions change as implied by the solutions shown in figs. 10 and 11. Figure 12 shows a snapshot of various contact fractions at $t = 150$ μs. The crack segments are color-coded based on a field of interest. For example in fig. 12(a) damage, $D \in [0,\ 1]$, is mapped to blue-to-red colors. The majority of cracks are at angles close to $\pm 45°$. Yet, six of them along the height of the domain run at around $+45°$ degree and form the major slip systems. These main cracks are almost entirely damaged across their lengths. The contact and slick relative fractions η and γ in fig. 12(b) and fig. 12(c) show that these planes are mostly in contact ($\eta \approx 1$) and in relative slip mode ($\gamma \approx 0$). The map of absolute slip mode a_{SL}, *cf.* (7b), in fig. 12(d) shows that there are some regions of active slip along these cracks. From the same figures, it is observed that the majority of connecting cracks between these main slip lines experience less damage and slippage.

Figure 13 shows the evolution of the front mesh, *cf.* §3, as cracks are nucleated and propagated in time. The time values shown in subfigure captions (second value), correspond to the lowest time coordinate of all vertices on the front. Since, the aSDG method is asynchronous, not all vertices have the same time coordinate; *cf.* fig. 7. The front mesh is modified to accommodate nucleation and propagation of cracks in arbitrary directions. In addition, adaptive operations ensure that the problem is solved with the desired level of accuracy. The latter point is demonstrated by the comparison of the initial front mesh in fig. 9 and the front meshes in figs. 13(a) and 13(b). While the initial front mesh is comprised of only two spatial elements, as the elastic waves enter the domain from the top and bottom boundaries, large energy dissipation in the bulk calls for refinement operations in the wave front. For this problem the wave front is not very sharp, since its thickness corresponding to the ramp time of 10 microseconds is 5.6 cm; *i.e.,* 35% of H. Still, as the load ramps up and enter the domain in figs. 13(a) and 13(b), more elements are created on the wave front and later inside the domain. The vertices encircled in these figures show local

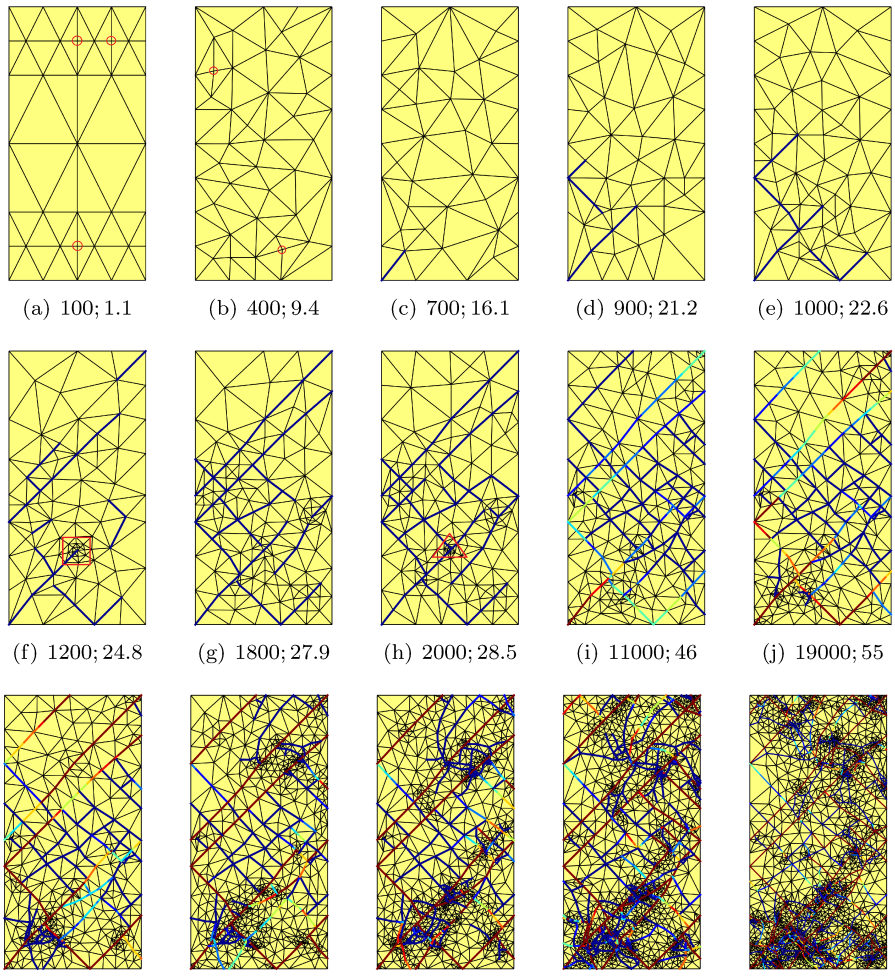

(a) 100; 1.1 (b) 400; 9.4 (c) 700; 16.1 (d) 900; 21.2 (e) 1000; 22.6

(f) 1200; 24.8 (g) 1800; 27.9 (h) 2000; 28.5 (i) 11000; 46 (j) 19000; 55

(k) 37300; 65 (l) 87000; 80 (m) 154000; 90 (n) 620000; 120 (o) $2.2M$; 150

Figure 13: The front mesh for the rock domain under uniaxial compressive load at different stages. Damage on crack segments in the range, $D \in [0,\ 1]$, is mapped to a blue-to-red color range. The first and second numbers in subfigure captions correspond to the total number of patches solved and minimum time coordinate of the vertices on the front mesh (in microseconds), respectively.

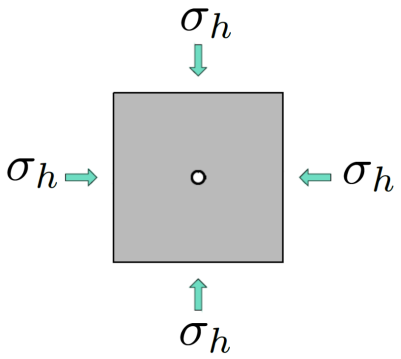

Figure 14: Problem sketch for compressive mode fracture problem.

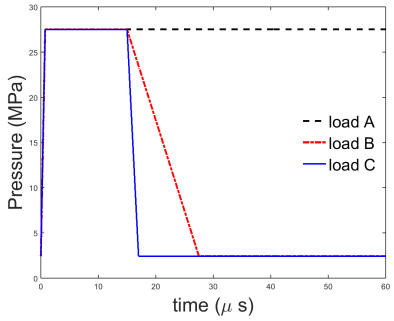

Figure 15: Load history for the compressive mode fracture problem.

edge bisection optionations on the front. The reader is referred to [59, 36] for the description of edge bisection and other mesh adaptivity operations.

Figures 13(c) to 13(e) show the propagation of cracks from the first three nucleation points. It is evident that the front mesh is very irregular and element boundaries are not aligned with $\pm 45^\circ$ directions. Local adaptive operations (mesh smoothing and refinement; *cf.* §3) are used to align element boundaries with proposed crack directions. This can more clearly be seen in the modification of the front mesh from fig. 13(e) to fig. 13(f). Given that the relaxation time $\tilde{\tau} = 30$ ms, it takes about 30 ms, until any visible damage accumulation can be observed on crack segments; see figs. 13(h) to 13(o).

Several adaptive operations on the front mesh are shown in fig. 13. The front mesh in rectangle and triangle zones in figs. 13(f) and 13(h) correspond to mesh adaptivity needed to accommodate requested crack direction and resolve local stress concentration points (relatively high strain energy densities and local slip can be observed in this triangle zone in fig. 10(a)). As local slip zones are activated and cracks propagate in figs. 13(j) to 13(o), corresponding to times shown in figs. 10(c) to 10(h), high energy dissipation error in the bulk, energy error on contact / fracture surfaces, and complex fracture pattern result in much finer front mesh. For example, the front mesh in fig. 13(o) contains 5682 elements and a total crack length of 3.44 m, which can be contrasted with 2 spatial elements and zero crack length for the initial front shown in fig. 9. Finally, it is noted that the aSDG mesh adaptive operations can capture other fracture angles that are implied either my using more appropriate failure criterion such as Mohr-Coulomb or by modeling anisotropic rock, as shown in [64].

4.2. Explosive fracturing

Consider a wellbore subjected to the ambient pressure $\sigma_h = 2.425$ MPa as shown in fig. 14. The diameter of the wellbore is 15.24 cm and the computational domain is 2 m $\times$ 2 m. The friction coefficient is $k = 0.3$. Similar to the problem

in §4.1, the domain initially does not contain any stress concentration points such as crack tips. Accordingly, the same statistical fracture nucleation and propagation model, based on Weibull distribution, is used for this simulation. The reader is referred to [65] for the model parameters. Also, instead of the effective stress model presented in §2.2.2, the effective stress is defined based on a Mohr-Coulomb failure criterion, which is more appropriate for fracture under compressive model, *i.e.,* when the normal traction on crack surfaces is compressive. The description of the effective stress model is provided in [65].

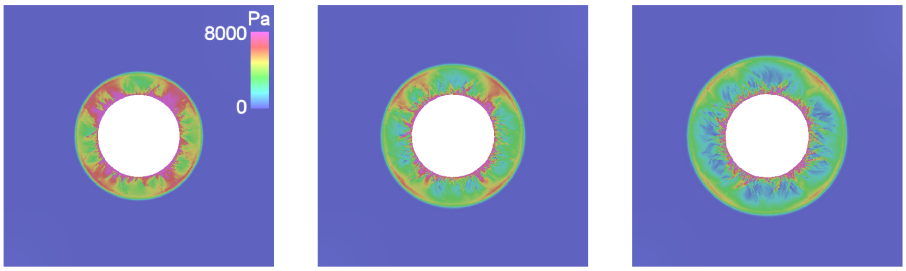

(a) Time $t = 15$ μs (b) Time $t = 20$ μs (c) Time $t = 25$ μs

(d) Time $t = 30$ μs (e) Time $t = 37.5$ μs (f) Time $t = 57.5$ μs

Figure 16: Strain energy density, mapped to color field, for the well fracture problem for load A (sustained loading).

As shown in fig. 15, three different load histories $\bar{p}(t)$, approximating an explosive load, are applied on the inner surface of the wellbore. For all the loads, the applied compressive pressure ramps from the ambient pressure to 27.5 MPa in 750 ns. In load A, $\bar{p}(t)$ is hypothetically maintained at this level afterward, while in loads B and C, the explosive load is released from time $t = 15$ μs. Load B corresponds to a slow unloading where the ambient pressure is recovered at $t = 27.5$ μs while for load C the unloading is complete at $t = 17$ μs. It is emphasized that these load histories are not taken from any real experiments and are simply chosen to demonstrate the effect of unloading rate (if any) on fracture pattern.

Figure 16 shows a sequence of solutions for load A. The high pressure from the explosive load compacts the rock around the wellbore and causes it to fail. The complex solution right around the wellbore is due to the nucleation and slant

propagation of cracks. The highly deformed shape of the wellbore boundary in fig. 16(e) and fig. 16(f) manifests the extend of rock compaction and failure in this zone. The outward propagating fronts of the circular compressive wave and fracture zone are relatively indistinguishable in fig. 16(a) to fig. 16(c). However, the distinction of these two fronts becomes more apparent in subsequent figures. This is contributed to two reasons. First, the compressive wave front propagates with the longitudinal wave speed c_{d}, *cf.* (1), which is considerably faster than the Rayleigh wave speed, the maximum attainable speed for the propagation of cracks for this problem set-up. Second, the relaxation time $\tilde{\tau}$ in the damage evolution model (8) causes a time delay from the time a crack is propagated to the time that it experiences partial or full damage.

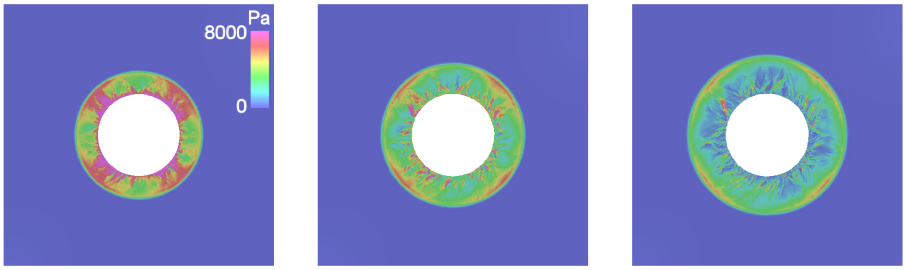

(a) Time $t = 15$ μs (b) Time $t = 20$ μs (c) Time $t = 25$ μs

(d) Time $t = 30$ μs (e) Time $t = 37.5$ μs (f) Time $t = 57.5$ μs

Figure 17: Strain energy density, mapped to color field, for the well fracture problem for load B (slow unloading).

The results for load B (slow unloading) are shown in fig. 17. The solution up to time $t = 15$ μs is exactly the same for all load cases, as the unloading in loads B and C starts from this time. This explains having identical results in fig. 16(a) and fig. 17(a) (and fig. 18(a)). The unloading, however, results in a relaxed stress field afterward. This is specifically evident at later times, *i.e.,* in fig. 17(d) to fig. 17(f) when the unloading is complete. This explains the low strain energy around the wellbore. The results for load C (fast unloading) are shown in fig. 18. Since the unloading occurs in 2 μs rather than 12.5 μs, the unloading wave front is much sharper for this case. The front of this unloading front can clearly be seen from fig. 18(b) to fig. 18(d). Interestingly, the strain

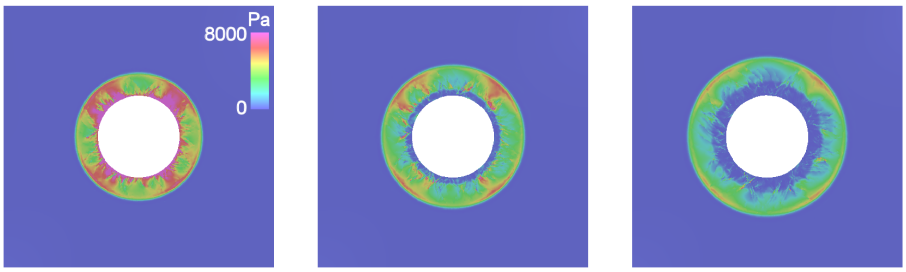

(a) Time $t = 15$ μs (b) Time $t = 20$ μs (c) Time $t = 25$ μs

(d) Time $t = 30$ μs (e) Time $t = 37.5$ μs (f) Time $t = 57.5$ μs

Figure 18: Strain energy density, mapped to color field, for the well fracture problem for load C (fast unloading).

energy (thus stress values) are further relaxed in the highly compacted zone around the wellbore in fig. 18(e) and fig. 18(f) compared to corresponding times in figs. 16 and 17.

Figure 19 shows the front mesh for load B at time $t = 37.5$ μs. The damage value D is shown on crack surfaces. As evident, only a short region around the wellbore is fully damaged. In fact, this is one of the potential drawbacks of explosive loading for stimulating a hydrocarbon reservoir, as the zone of fractured rock—while being more damaged—is often not as expansive as that corresponding to hydraulic fracturing. The long propagation of cracks is caused by the passage of the compressive wave around the wellbore. However, the duration of sufficiently high stress values farther than the wellbore is not long enough, compared to $\tilde{\tau}$ in (8), to induce full damage. This is due to the decreasing intensity of the compressive wave as its front moves farther outward. Finally, it is noted that mesh adaptivity again captures sharp moving wave fronts and follows the regions of high crack density in the damaged zone; for example the mesh adaptivity is more modest in the upper left side of the wellbore where the the crack density is lower.

The damage values and crack patterns for the three different load cases are compared in fig. 20 at time $t = 37.5$ μs. Similar to load A, only a small region around the wellbore is fully damaged for load cases B and C. Also, there is not a significant difference in the extend of both crack propagation and fully damaged

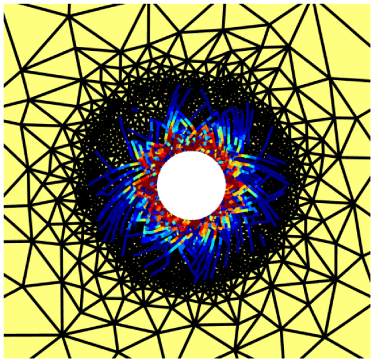

Figure 19: The front mesh for the well fracture problem for load B at time $t = 37.5$ μs. Damage on crack segments in the range, $D \in [0,\ 1]$, is mapped to a blue-to-red color range.

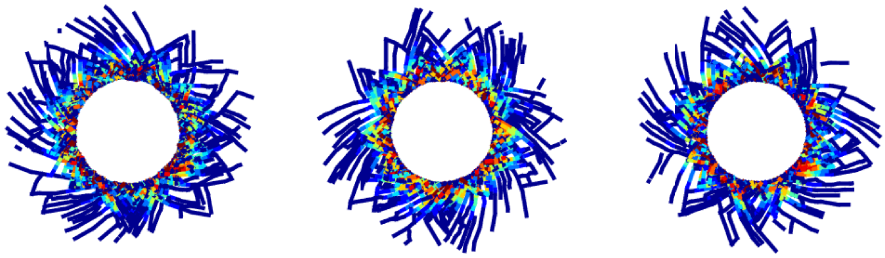

(a) A (sustained loading). (b) B (slow unloading). (c) C (fast unloading).

Figure 20: Comparison of crack patterns and damage values for different applied loadings at time $t = 37.5$ μs. Damage values on crack segments in the range $D \in [0, 1]$ map to a blue-to-red color range.

regions among difference load cases. Finally, fig. 21 shows the contact–slip area a_{SL}, *cf.* §2.2.1. For load cases A and B, the damaged region around the wellbore is mostly in contact–slip mode, verifying the fact that cracks mostly propagate in a shear mode dominant fashion. However, in fig. 21(c) the regions with high contact–slip area have considerably shrunk. This is contributed to the long (about 20 μs) time past since the unloading of the compressive load.

4.3. Hydraulic pressure regularization

Figure 22 shows the schematic of a problem where a hydraulically loaded fracture intersects a vertically oriented unloaded natural fracture. To illustrate the effect of pressure regularization from §2.2, the problem is first solved without the regularization followed with a solution with regularization active. The hydraulic pressure p_h ramps up from the ambient pressure of 2.425 MPa to the sustained value of 19.4 MPa in 1 microseconds. The long in-situ crack length and short ramp time in the application of hydraulic load are chosen to better

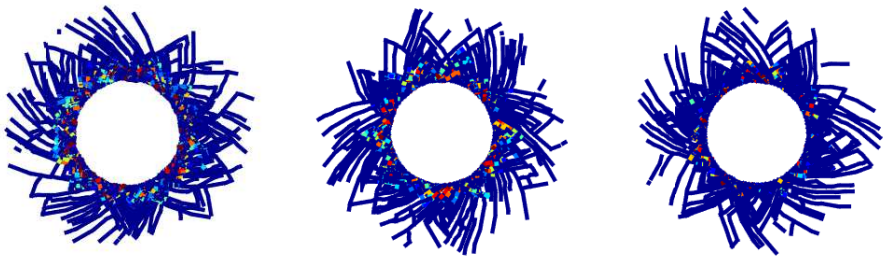

(a) A (sustained loading). (b) B (slow unloading). (c) C (fast unloading).

Figure 21: Comparison of crack patterns and contact–slip area for different applied loadings at time $t = 37.5$ μs. Contact-slip areas on crack segments in the range $a_{\mathrm{SL}} \in [0, 1]$ map to a blue-to-red color range.

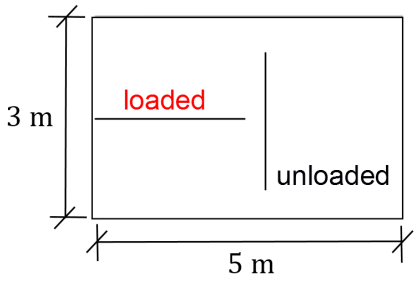

Figure 22: Sketch of the problem for modeling the interaction of a hydraulically-loaded horizontal crack with an unloaded in-situ vertical crack.

demonstrate the problems with the sudden transfer of hydraulic load. In addition, to focus only on these two cracks, the crack nucleation is intentionally deactivated in these two problems. This prevents the penetration of the hydraulic crack through the vertical crack or potential nucleation of new cracks from these cracks or other points in the domain.

Figure 23 and 24 show sequences of solutions and front meshes when the pressure is not regularized. Similar to previous elastic solution visualizations, strain energy density is mapped to color field. In addition, kinetic energy density is mapped to height field for the remainder of solution visualizations. Figure 24 shows the spatial fronts from different instants of the aSDG solution. Figure 23(a) shows the instant right before the hydraulically loaded crack intersects the in-situ crack. The color field around the tips of the vertical crack represents the strain field generated due to the scattering of elastic fields by these points. As shown in fig. 24(a), the vertical crack is still unloaded ($f_p = 0$). Figures 23(b) to 23(e) show a time period of less than 6 μs where the entire length of the in-situ crack is fully loaded. Two problems arise with non-regularized transmission of the hydraulic load. First problem is the sudden jump in the hydraulic pressure acting on the intersected cracks. At the time of intersec-

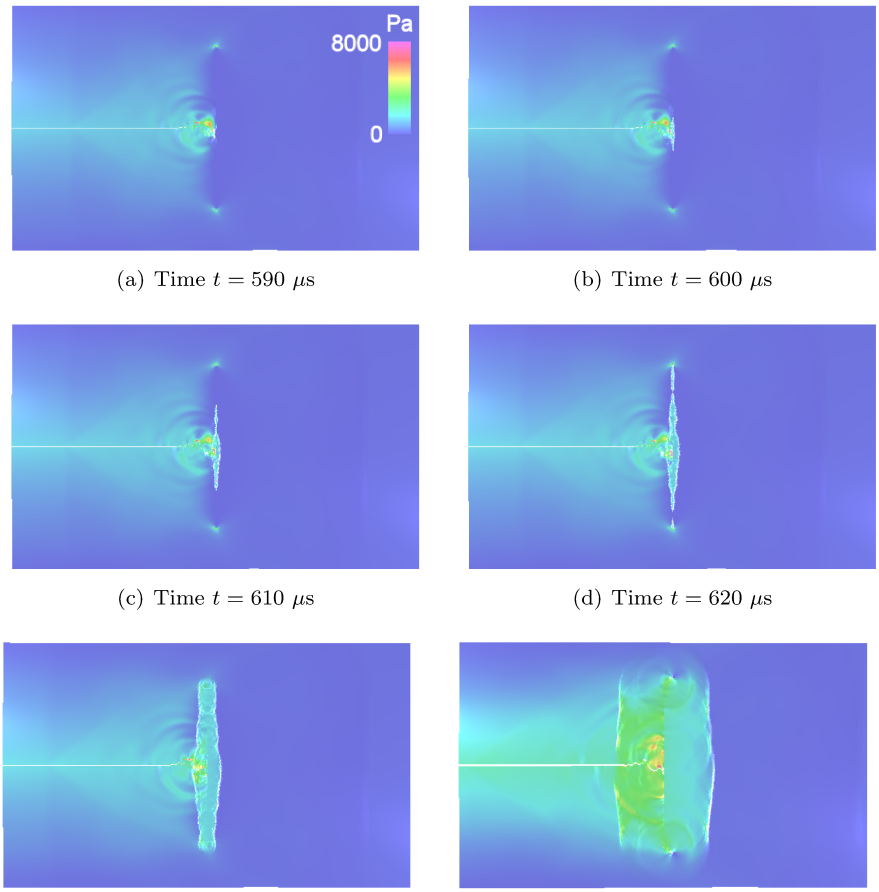

(a) Time $t = 590$ μs

(b) Time $t = 600$ μs

(c) Time $t = 610$ μs

(d) Time $t = 620$ μs

(e) Time $t = 650$ μs

(f) Time $t = 800$ μs

Figure 23: Strain and kinetic energy densities, mapped to color and height fields respectively, for the problem in fig. 22 without pressure regularization. Lack of pressure regularization results in sharp jumps in stress and velocity.

tion, which is roughly at 600 μs, hydraulic pressure is $p_h \approx 12.6$ MPa. That is, upon intersection the pressure instantly jumps from the ambient pressure of 2.425 MPa to $p_h \approx 12.6$ MPa. The spikes in fig. 23(b) to fig. 23(d) correspond to a sudden jump in material velocity field induced by instantaneous application of the hydraulic load. The second problem is that the entire crack line experiences the hydraulic load right at the time of intersection, *cf.* fig. 23(b) to fig. 23(e). Aside from these nonphysical responses, the non-regularized application of hydraulic load significantly increases the computational cost; the very high level of mesh refinement in fig. 24(b) to fig. 24(d) corresponds to the sharp wave fronts generated by the sudden change in the pressure load applied on the vertical crack. The refinement lines track the wave fronts that carry the high amplitude compressive waves in the bulk. These sharp wave fronts, and the corresponding

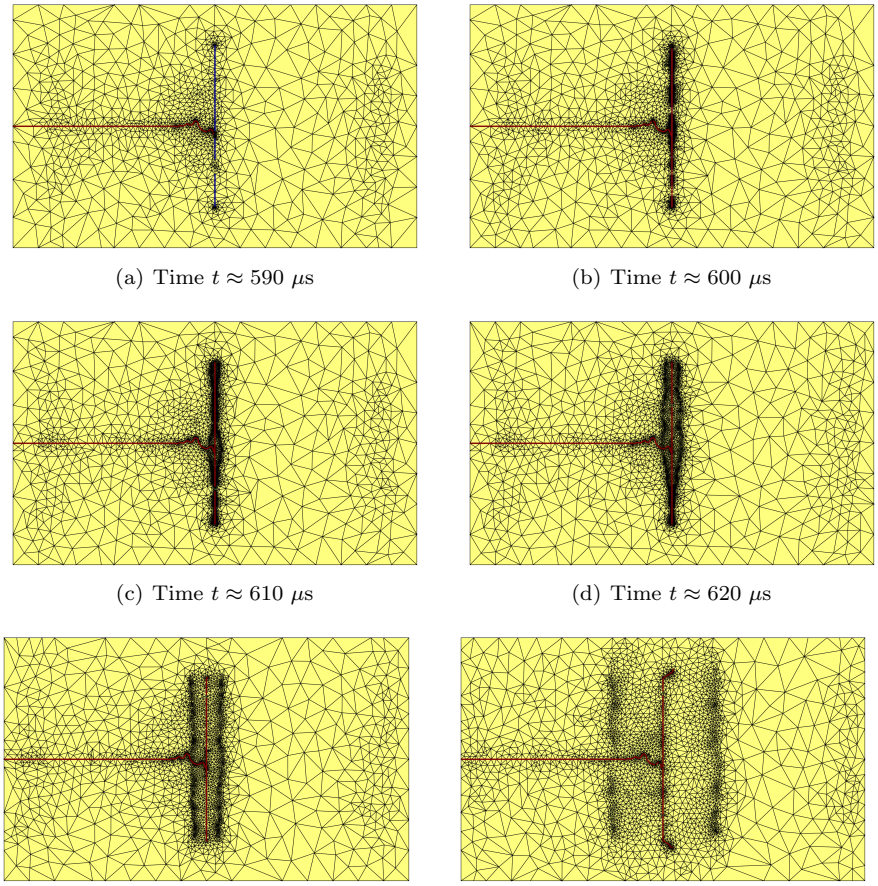

(a) Time $t \approx 590$ μs

(b) Time $t \approx 600$ μs

(c) Time $t \approx 610$ μs

(d) Time $t \approx 620$ μs

(e) Time $t \approx 650$ μs

(f) Time $t \approx 800$ μs

Figure 24: A sequence of front meshes at different times for the problem in fig. 22 without pressure regularization. Pressure factors on crack segments in the range, $f_p \in [0,\ 1]$, are mapped to a blue-to-red color range.

refinement lines, can be observed at a later time in fig. 23(f) and fig. 24(f).

For the second problem we use a parameter $\delta'_P = 0.1$, *cf.* (16), to demonstrate the effect of pressure regularization. Figures 25 and 26 show the solution and the front meshes for six different stages of the problem, respectively. Figure 25(a) shows a time slightly before the intersection of the cracks. The value of $f_p = 0$ on the vertical line in 26(a) confirms that the cracks have not intersected. The slight oscillation of the propagating crack is commonly observed in dynamic fracture of quasi-brittle materials as it provides a means to dissipate excess input energy to the system. Figure 25(b) shows an instant slightly after the hydraulically crack intersects the in-situ crack. During the process at which a point on the in-situ crack transitions from fully unloaded ($f_p = 0$) to fully loaded ($f_p = 1$), pressure increases from the in-situ stress (2.425 MPa) to the

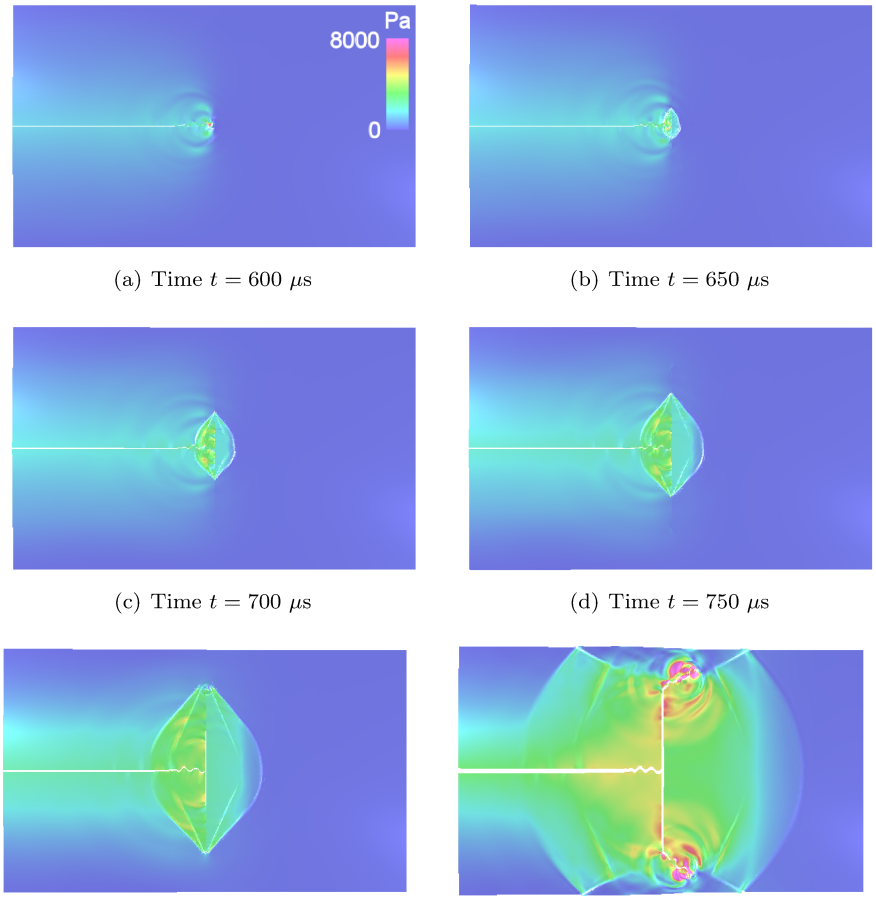

(a) Time $t = 600$ μs

(b) Time $t = 650$ μs

(c) Time $t = 700$ μs

(d) Time $t = 750$ μs

(e) Time $t = 820$ μs

(f) Time $t = 1.2$ ms

Figure 25: Strain and kinetic energy densities, mapped to color and height fields respectively, for the problem in fig. 22 with pressure regularization.

instantaneous hydraulic pressure of 12.6 MPa at time $t \approx 600$ μs or higher at later times. Although this process is regularized by the process described in §2.3, and eliminated the nonphysical responses observed in fig. 23 and fig. 24, it still creates high gradient wave fronts. This can be observed in fig. 26(b) where the two *hydraulic pressure process zone tips* separate the *hydraulic pressure process zone* from the unloaded parts of the in-situ crack.

Figures 25(b) to 25(e) show the propagation of hydraulic load on the vertical crack in the time span of about 170 μs. As can be seen the sharp transition of mechanical waves and their outward motion on the in-situ crack generates diagonal waves in the bulk. The mesh adaptivity in figs. 26(b) to 26(e) captures these solution features by creating finer elements at the tips of the process zone and along the diagonal waves. Also, the change of $f_p = 1$ inside the hydraulic pressure process zone to $f_p = 0$ outside of it, confirms the gradual application

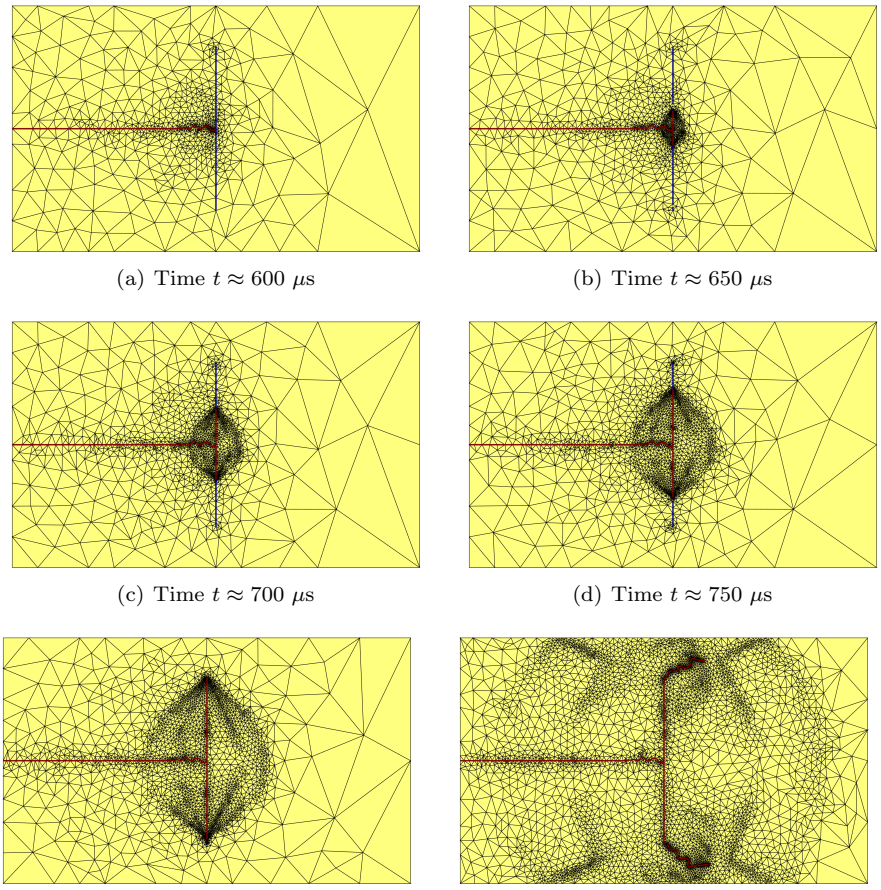

(a) Time $t \approx 600$ μs

(b) Time $t \approx 650$ μs

(c) Time $t \approx 700$ μs

(d) Time $t \approx 750$ μs

(e) Time $t \approx 820$ μs

(f) Time $t \approx 1.2$ ms

Figure 26: A sequence of front meshes at different times for the problem in fig. 22 with pressure regularization. Pressure factors on crack segments in the range, $f_p \in [0,\ 1]$, are mapped to a blue-to-red color range.

and propagation of the hydraulic load. Finally, figs. 25(f) and 26(f) correspond to a time after the hydraulic pressure reaches the tips of the vertical crack. The hydraulic load extends these cracks into the bulk. As evident from these two examples, pressure regularization smoothens out an otherwise sudden application of hydraulic load and prevents it instantaneous propagation along the length of in-situ cracks. As a final note for these two problems, the high level of dynamic mesh adaptation in figs. 24 and 26 is needed to capture complex fracture patterns and solve solution features such as sharp wave fronts and contact and slip lines accurately. Moreover, mesh coarsening operations behind moving fracture process zones and wave fronts are essential to keep the computational costs manageable. These adaptive operations are discussed in more detail in §3, §4.1, and [36, 62].

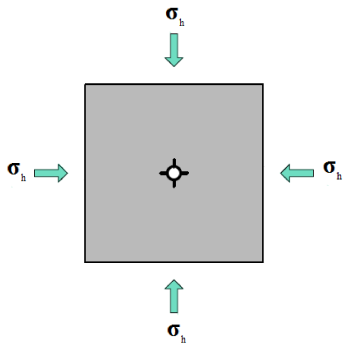

Figure 27: Problem description of a wellbore with four perforations.

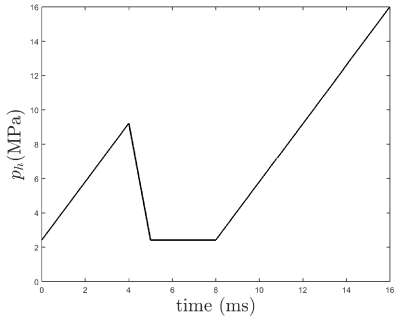

Figure 28: Load history for the hydraulic re-fracturing problem.

4.4. Contact and re-fracture in hydraulic fracturing

Before presenting the remaining numerical results, which are pertained to hydraulic fracturing, we point out that aside from the modifications implied by pressure regularization, a spatially uniform hydraulic pressure p is exerted on all hydraulically loaded crack surfaces. That is, p is not obtained from a fluid model such as the lubrication equation. However, as detailed in [61] and in the beginning of §2.3, this assumption is reasonably accurate in many circumstances. In any case, the focus of the subsequent examples is on incorporating Riemann contact solutions for hydraulic fracturing applications. Even if required, they can be included in more advanced fluid models, an aspect that is beyond the scope of this manuscript.

Figure 27 shows the problem set-up for a wellbore with 4 perforations, at $0°, 90°, 180°, 270°$ angles. The 16 m $\times$ 16 m domain is under uniform ambient pressure $\sigma_h = 2.425$ MPa. The hydraulic pressure history is shown in 28. The purpose of this example is to demonstrate that the regularization of η from §2.2.3 smoothens the transition of a hydraulically loaded crack from separation to contact mode when hydraulic load is removed and to use the pressure factor

concept from §2.3 to gradually re-apply hydraulic pressure on already fractured segments. Similar to previous problems, the loads are applied rapidly to better demonstrate various contact and load transition modes.

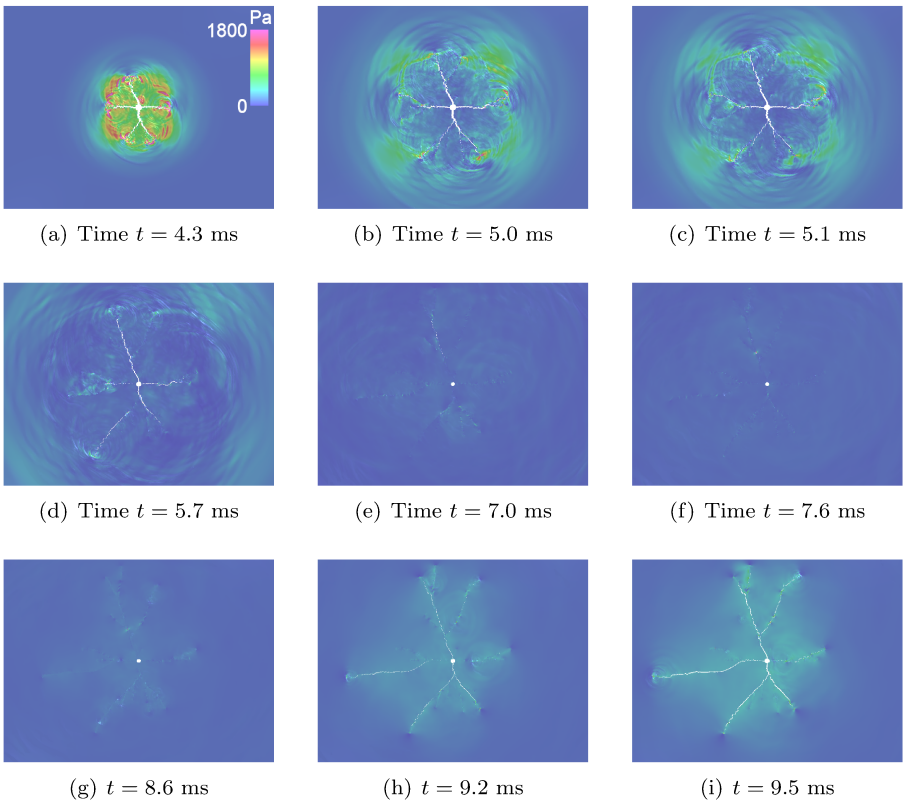

(a) Time $t = 4.3$ ms (b) Time $t = 5.0$ ms (c) Time $t = 5.1$ ms

(d) Time $t = 5.7$ ms (e) Time $t = 7.0$ ms (f) Time $t = 7.6$ ms

(g) $t = 8.6$ ms (h) $t = 9.2$ ms (i) $t = 9.5$ ms

Figure 29: Strain and kinetic energy densities, mapped to color and height fields respectively, for the hydraulic re-fracturing problem.

Figures 29 and 30 show the aSDG solution and space mesh for different stages of this hydraulic re-fracturing problem. In addition, in fig. 30 we map pressure factor f_p to color on fracture segments to discuss its evolution in time. Figures 29(a) and 30(a) show the solution and mesh in the early stages of the period when the hydraulic load is being removed. The existence of regions of high kinetic and strain energy densities, mapped to height and color fields respectively, corresponds to a highly transient crack propagation regime. The diagonal short crack between the right and top main cracks propagates in shear mode and is not hydraulically loaded; *cf.* fig. 30(a) where $f_p = 0$. The propagation of this crack is induced by scattered waves and stress redistribution. Other than this, all the other cracks are hydraulically loaded and propagate in a tensile-dominated mode.

Figures 29(b) and 30(b) correspond to $t = 5$ ms where the hydraulic pressure is completely removed. As a result, we already observe some microcracks start

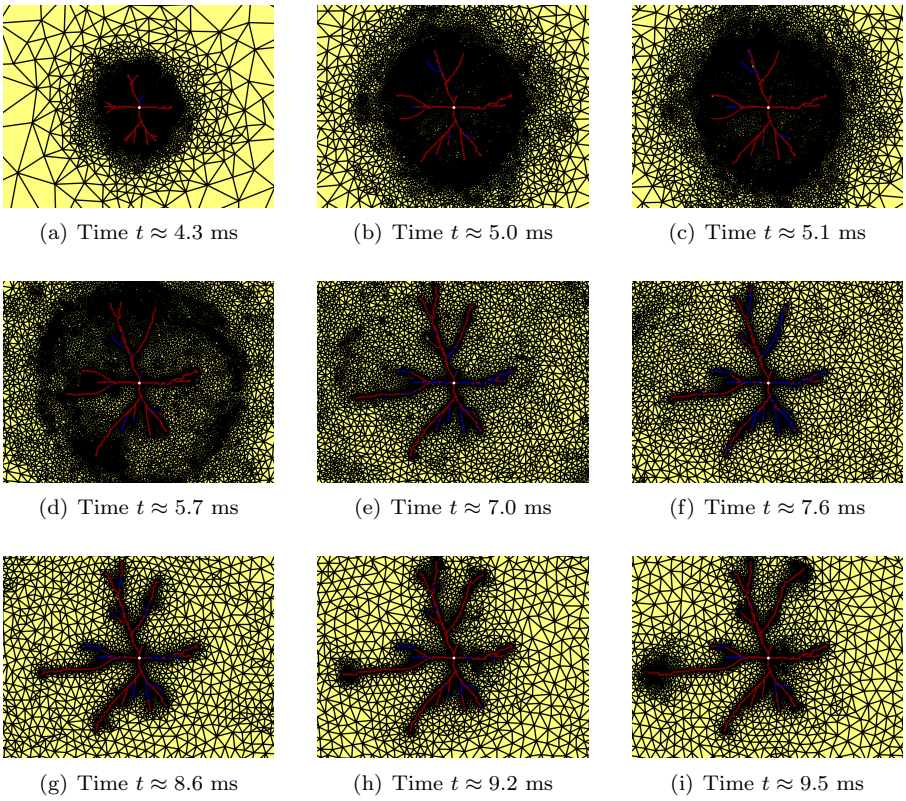

(a) Time $t \approx 4.3$ ms (b) Time $t \approx 5.0$ ms (c) Time $t \approx 5.1$ ms

(d) Time $t \approx 5.7$ ms (e) Time $t \approx 7.0$ ms (f) Time $t \approx 7.6$ ms

(g) Time $t \approx 8.6$ ms (h) Time $t \approx 9.2$ ms (i) Time $t \approx 9.5$ ms

Figure 30: A sequence of front meshes at different times for the hydraulic re-fracturing problem. Crack segments are colored based on the value of pressure factor f_p with blue to red corresponding to the range $f_p \in [0\ 1]$.

to transition to contact mode with the microcrack on the top left side of the vertical main crack being one example. Figures 29(c-d) and 30(c-d) refer to times slightly after the removal of the hydraulic load. We observe that the crack surfaces start to close. See for example the closure of the horizontal crack segment at the far left end of the left main crack. Local wave scattering events and the transition of f_p to zero can be seen in figs. 29(c) and 30(c). Another interesting observation is the emittance of acoustic waves in all directions as a result of crack and microcrack closures. The front of these secondary waves can more clearly be seen in figs. 29(d) and 30(d).

Figures 29(e-f) and 30(e-f) show the transition of the remaining crack surfaces to contact mode. The progression of regions with complete crack closure and $f_p = 0$ can be observed in the figures. It should be emphasized that the regularization of η, *cf.* fig. 5, is essential in smooth separation to contact mode transition. Also, the low level of mesh refinement in fig. 30(e-f), compared to previous times, stems from the fact that the entire domain is reverting to its spatially uniform ambient pressure field.

Load case	$\dot{p}$	$P_2(t, p_h)$
A	14.55 GPa/s	500 μs, 12.125 MPa
B	1.455 GPa/s	500 μs, 5.578 MPa
C	145.5 MPa/s	500 μs, 4.923 MPa
D	14.55 MPa/s	500 μs, 4.8573 MPa

Table 1: The loading rate and distinct points in load history of four loading cases considered for the refracturing problem in fig. 31. The other points $P_1(0\ \mu\text{s}, 4.85\ \text{MPa})$, $P_3(1\ \text{ms}, 2.425\ \text{MPa})$, and $P_4(2\ \text{ms}, 2.425\ \text{MPa})$ are the same for all load histories.

Finally, in figs. 29(g-i) and 30(g-i) the cracks start to transition back to separation mode after the start of the second stage of hydraulic loading from $t = 8$ ms. Specifically, in the space meshes we observe the progression of f_p from zero to one for all cracks except a few microcracks that remain arrested and in contact. As expected, cracks further open and propagate in tensile-dominated mode due to hydraulic loading. One key aspect of the model for transition from contact to separation mode is the use of the aperture of all connected segments to a crack segment, rather than only the crack itself (that is using cracks CA, BE, and AD in fig. 6 in computing f_p for crack segment AB), in computing $\delta_{P_{\max}}$ in (15) and subsequently f_p in (16). This results in natural propagation and re-application of hydraulic load from the main four initial perforations outward to other cracks. Otherwise, all crack segments would remain in contact mode given that their opening does not increase in the absence of hydraulic pressure.

4.5. Effect of loading rate and interaction with in-situ cracks

Figure 31 shows the problem set-up for a wellbore with 4 perforations, with domain size and perforation angles similar to the problem in fig. 27. The difference is the presence of in-situ cracks with crack density 0.5[2]. The microcrack lengths follows a Weibull distribution. A take-and-place algorithm is used to place them in the computational domain. Their angles follow a uniform distribution with mean value and range of 30° and 10°, respectively.

The purpose of this example is to demonstrate the effect of hydraulic loading rate in fracture / refracture response and to study the interaction of hydraulically loaded cracks with in-situ cracks. Four loading rates $\dot{p}$ are used for the loading stages of hydraulic fracturing in this problem. The load histories for load cases A to D are shown in fig. 32. Since the times of unloading and reloading at positions P_2 and P_3 do not change, the only difference between these simulations arise in how fast the load ramps up. The load history parameters are compared in Table 1. As can be seen, each time the loading rate decreases by a factor of 10 from load A to load D. While the high loading rates, for example for loads A and B, can be deemed unrealistic in conventional hydraulic fracturing practices,

[2]Crack density is the nondimensional number defined by sum of squares of crack lengths per unit area of the domain.

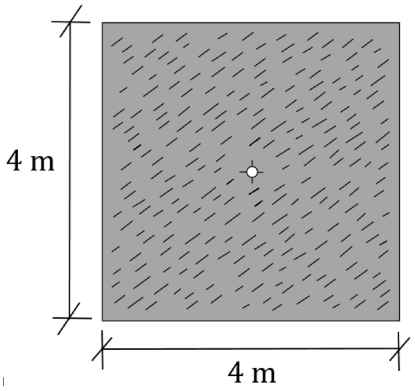

Figure 31: Problem description of a wellbore with four perforations, surrounded by in-situ cracks with density 0.5 and 30° angular bias.

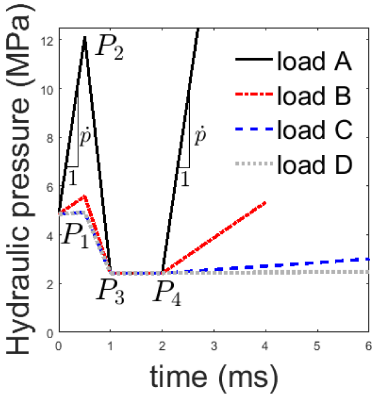

Figure 32: Load history for the refracture problem with in-situ cracks.

this example demonstrate how the crack patterns are altered when the loading rate decreases.

Figure 33 shows the results for load A. Figures 33(a) and 33(b) show the response in the first loading stage. In fact, the unloading starts right from $t = 500$ μs in fig. 33(b). The high strain and kinetic energies are due to the high value of $\dot{p}$. The microcracks have a minor effect in changing the crack paths during this stage due to the high crack propagation driving force. More importantly, all four perforations result in crack propagation.

As hydraulic load starts to decrease from fig. 33(b), crack paths start to be further affected by in-situ crack directions. This is more in the form of crack path alignment for the cracks emanating from 0^0 and 180° perforations, as the angle difference between propagating and in-situ cracks is around 30°. Examples of such alignments can be seen on the right propagating crack in

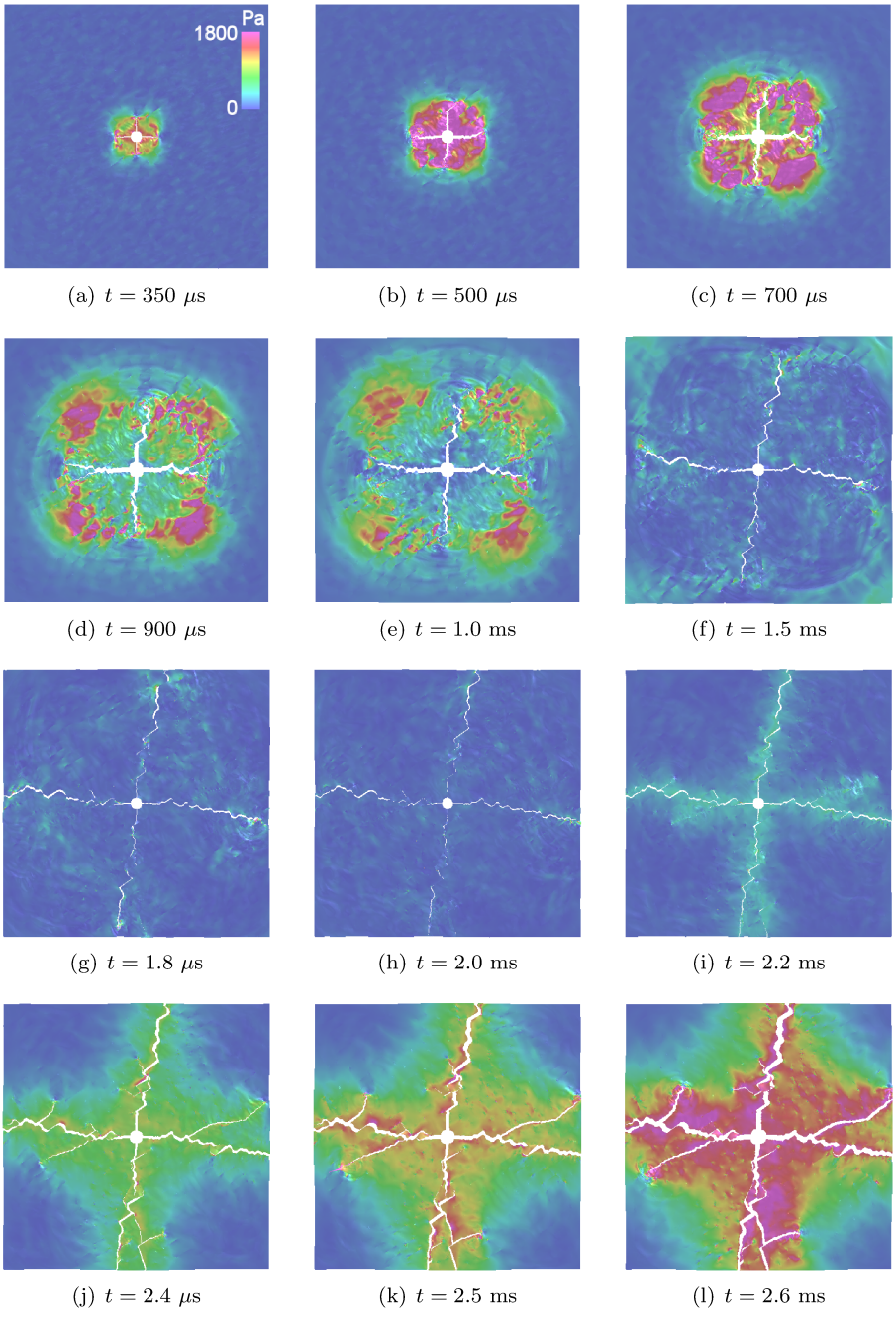

(a) $t = 350$ μs (b) $t = 500$ μs (c) $t = 700$ μs

(d) $t = 900$ μs (e) $t = 1.0$ ms (f) $t = 1.5$ ms

(g) $t = 1.8$ μs (h) $t = 2.0$ ms (i) $t = 2.2$ ms

(j) $t = 2.4$ μs (k) $t = 2.5$ ms (l) $t = 2.6$ ms

Figure 33: Strain and kinetic energy densities, mapped to color and height fields respectively, for the hydraulic re-fracturing problem with domain description in fig. 31 for load A ($\dot{p} = 14.55$ GPa/s).

fig. 33(b) and fig. 33(c). For vertically propagating cracks, however, the angle difference appears to be too high for alignment in most cases, and the in-situ cracks tend to offset the path of the propagating cracks. Examples can be found on the upward propagating crack in fig. 33(b) to fig. 33(d).

The unloading of the hydraulic pressure releases the stress, thus the internal energy, in the bulk. The initiation of these lower energy regions close to the bases of the perforations and their propagation outward can be seen in fig. 33(b) to fig. 33(d). As this lower energy zone expands, its interaction with in-situ cracks creates a complex stress field. This can more clearly be seen in fig. 33(d) and fig. 33(e) and is the source of minor stress variations at later stages in fig. 33(f) to fig. 33(h).

The propagation of crack in the unloading stage, *i.e.,* fig. 33(b) to fig. 33(e), is expected as the hydraulic load is still large enough to continue driving crack propagation. For this highly dynamic loading crack propagation continues (at lower speeds) even during the stage where the hydraulic load is completely released; *i.e.,* from fig. 33(e) to fig. 33(h). This is due to the highly dynamic nature of loading. In fact, crack surfaces are not even fully closed at the end of unloading stage in fig. 33(e) and more time would have been needed for this to happen. Some exceptions can be seen on the side microcracks, *e.g.,* the cracks that are roughly along 30° on the lower and upper sides of the left- and right-propagating main cracks, respectively, in fig. 33(f) and fig. 33(g). In fact, from the instant the second loading stage starts in fig. 33(h) to fig. 33(l) besides these two cracks, many other microcracks (nucleate and) start propagating close to 30°.

The results for load B are shown in fig. 34. We observe a much subdued internal energy field up to the ends of loading and unloading stages in fig. 34(b) and fig. 34(d), respectively. In addition, only three of the perforations result in hydraulic crack growth; the two left- and right-propagating cracks have a more favorable path as their angles are closer to the in-situ crack directions. Due to the lower loading rate $\dot{p}$, not only energy fields decrease but also only one of the two vertical cracks (the lower one) propagates. In fact, this crack has a smaller overall opening and closes between $t = 700$ μs to $t = 1.4$ ms (*cf.* figs. 34(c) to fig. 34(e)), before the horizontal cracks close. Moreover, due to the lower rate of loading in this case, all the cracks are completely in contact mode before the second loading stage starts at $t = 2$ ms; *cf.* fig. 34(f). The nonuniform stress field implied by the color map is a result of wave scatterings off of in-situ cracks during the unloading stage. The crack propagation in the second stage of loading is shown in fig. 34(g) to fig. 34(i). Due to the lower driving force for the cracks, their path is more affected by in-situ cracks. This particularly holds true for the vertical crack where at least three crack path diversions can be seen in fig. 34(i).

The results for load C are shown in fig. 35. In comparison to the results for load B, we observe a much less dynamic mode of crack propagation (implied by lower energy fields). In addition, no vertical cracks propagate in this case. The elimination of active propagation directions from the initial perforations is a result of decreased power input to the system. From an energetic perspective,

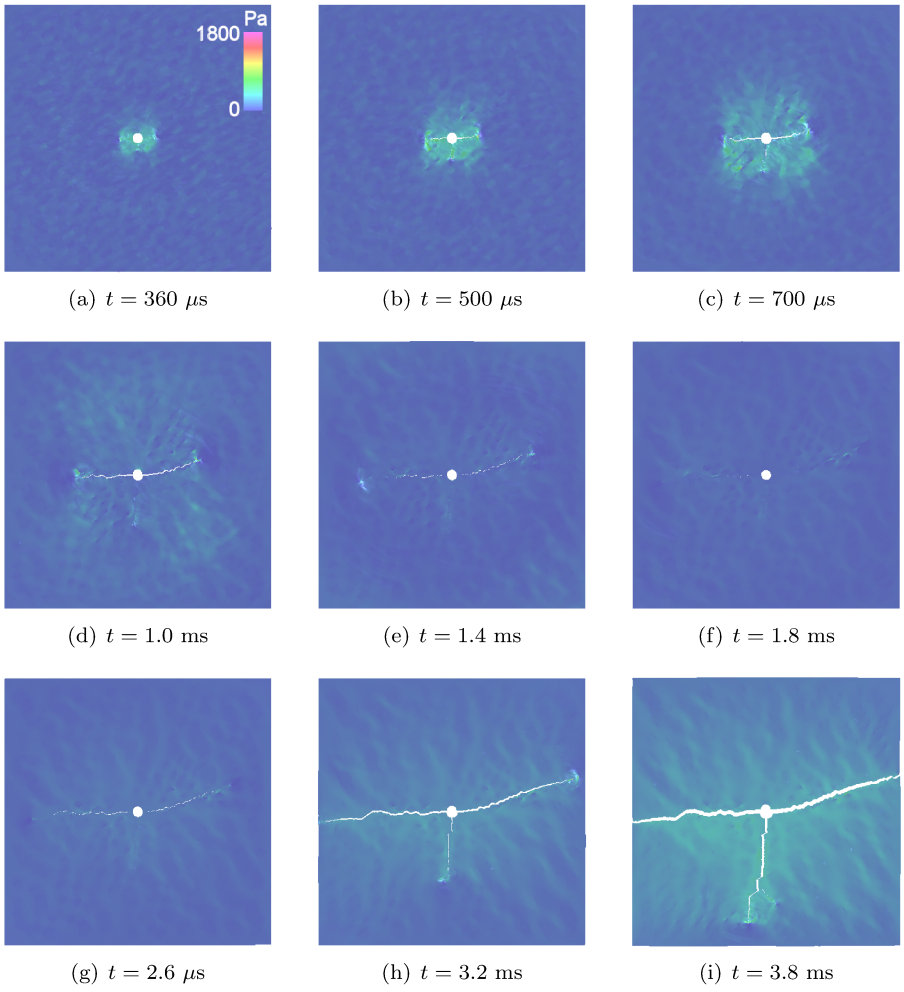

(a) $t = 360$ μs (b) $t = 500$ μs (c) $t = 700$ μs

(d) $t = 1.0$ ms (e) $t = 1.4$ ms (f) $t = 1.8$ ms

(g) $t = 2.6$ μs (h) $t = 3.2$ ms (i) $t = 3.8$ ms

Figure 34: Strain and kinetic energy densities, mapped to color and height fields respectively, for the hydraulic re-fracturing problem with domain description in fig. 31 for load B ($\dot{p} = 1.455$ GPa/s).

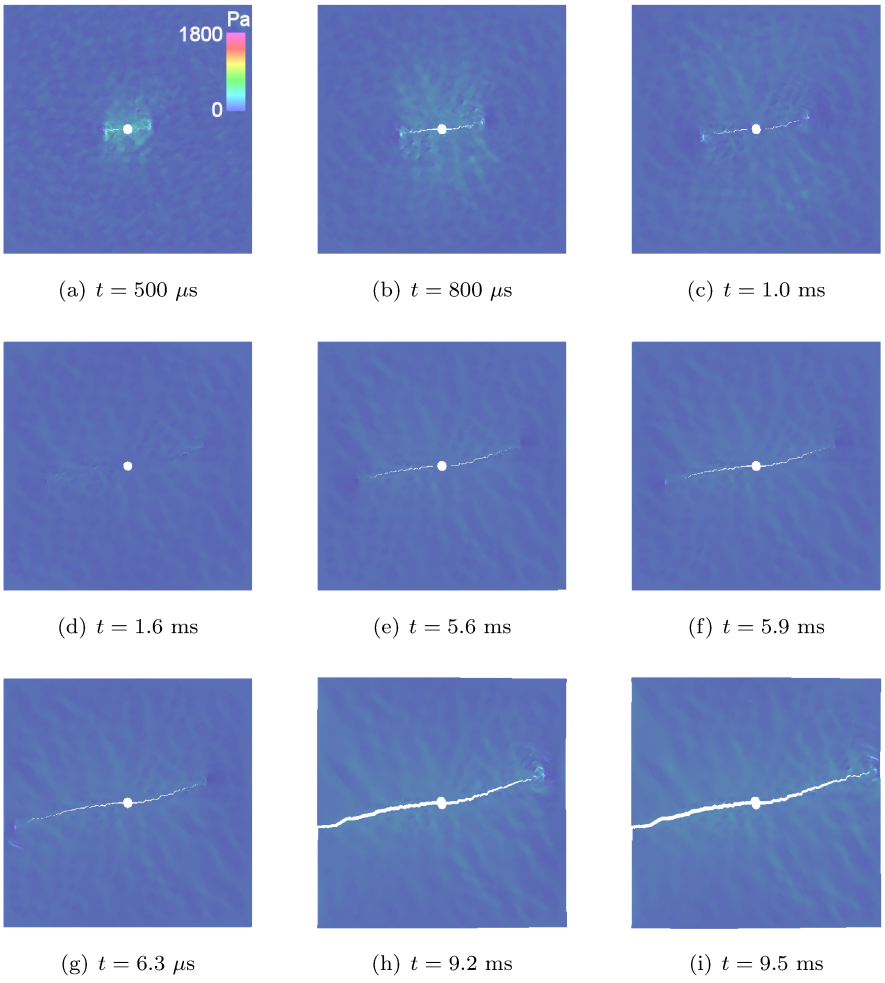

(a) $t = 500$ μs (b) $t = 800$ μs (c) $t = 1.0$ ms

(d) $t = 1.6$ ms (e) $t = 5.6$ ms (f) $t = 5.9$ ms

(g) $t = 6.3$ μs (h) $t = 9.2$ ms (i) $t = 9.5$ ms

Figure 35: Strain and kinetic energy densities, mapped to color and height fields respectively, for the hydraulic re-fracturing problem with domain description in fig. 31 for load C ($\dot{p} = 145.5$ MPa/s).

the propagation of the two horizontal cracks in this case suffices to dissipate the input energy to the system. Herein, the propagation of the horizontal cracks rather than vertical ones is a result of their favorable interaction with in-situ cracks. This phenomena is also reported in [66] for simpler loading and geometry settings. For this problem, the crack closure occurs at an earlier time when the hydraulic load is released; *cf.* fig. 34(f) and fig. 35(d). Moreover, the resumption of crack propagation takes a much longer time due to the lower rate of loading.

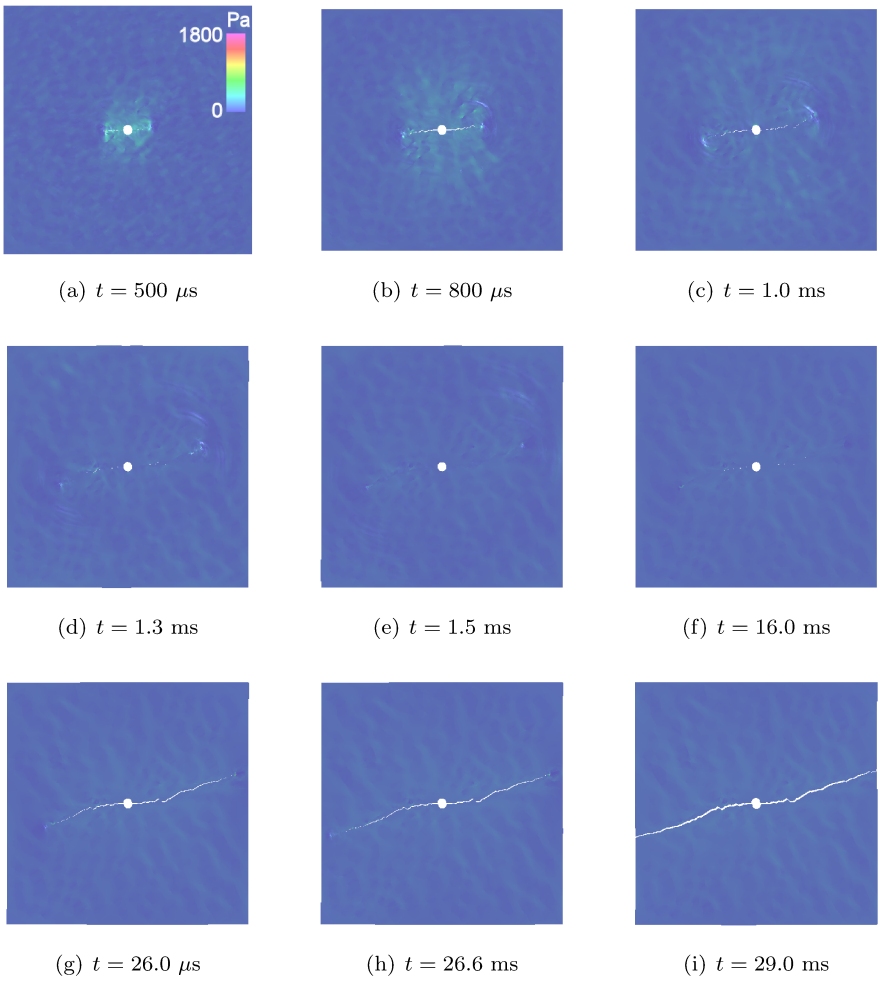

(a) $t = 500$ μs (b) $t = 800$ μs (c) $t = 1.0$ ms

(d) $t = 1.3$ ms (e) $t = 1.5$ ms (f) $t = 16.0$ ms

(g) $t = 26.0$ μs (h) $t = 26.6$ ms (i) $t = 29.0$ ms

Figure 36: Strain and kinetic energy densities, mapped to color and height fields respectively, for the hydraulic re-fracturing problem with domain description in fig. 31 for load D ($\dot{p} = 14.55$ MPa/s).

The results for load D are shown in fig. 36. The same trends described for load C continue and are enhanced for this lower loading rate. In fact, crack clo-

sure is complete in fig. 36(d), just slightly after the hydraulic load is completely released in fig. 36(c). The resumption of crack propagation also takes a much longer time, as can be seen in fig. 36(f).

One very important observation for the crack propagation under these lower loading rates is the occurrence of rather short periods at which long crack propagations are observed. For example, between fig. 36(g) to fig. 36(h) (and beyond that fig. 36(i)) we observe significant crack propagation in a rather short time relative to the loading period. These bursts become more dynamic at higher loading rates, see for example crack propagations between fig. 35(h) to fig. 35(i) and fig. 34(h) to fig. 34(i) for loads B and C, respectively. The height and color fields around these moving cracks imply that the crack propagation during these short periods has some dynamic characteristic. The reason for this behavior is that once the stress field around the a crack tip builds sufficiently high (though slow increase of the hydraulic load), the crack propagation suddenly becomes favorable. For this particular problem where cracks interact and get arrested by in-situ cracks there are more instances of such short periods of crack propagation. In fact, their acoustic wave signature may be large enough to enable the detection of crack propagation.

5. Conclusions

We presented an interfacial damage model for dynamic rock fracturing and hydraulic fracturing applications that seamlessly combines separation, contact–stick, and contact–separation modes. The employed Riemann solutions preserve the characteristic structure of elastodynamic waves for different contact modes. As demonstrated the separation-to-contact separation is physically non-smooth. We proposed a regularization approach that smoothened separation-to-contact mode transition in the presence of nonzero fracture surface loads, *e.g.,* hydraulic fracturing pressures. Moreover, the contact-to-separation transition is typically smooth; however, when a hydraulically loaded crack intersects an in-situ crack, this transition is nonsmooth as well. We proposed an aperture-based regularization scheme that smoothens the application of hydraulic load under such conditions.

Numerical results demonstrate the effectiveness of the proposed methods in modeling various crack interaction scenarios. The uniaxial compressive loading and wellbore explosive examples demonstrate that the stochastic nucleation and h-adaptive aSDG method can capture complex formation and propagation of cracks under highly dynamic loads. Various contact mode transitions, particularly between stick and slip modes, were observed in these examples. For the refracture examples, we showed that the pressure regularization not only smoothens out the application of hydraulic load but also prevents its nonphysical and sudden application on the entire length of a newly intersected crack. Simple refracture examples demonstrated the ability of the method to model crack closure and re-opening under the removal and reapplication of the hydraulic load. We also demonstrated that as the loading rate decreased, fewer

perforations in a wellbore became active, and those that had a more favorable orientation relative to in-situ cracks remained active.

Some future works for more accurate modeling of the aforementioned problems are the derivation of fluid pressure on fracture surfaces from a fluid model, formulation of dynamic contact solutions for poroelastic rock, and more realistic modeling of refracture problem. Pertained to the the last point, the refracture problems in §4.5 are more naturally modeled when different flow rate profiles, rather than pressure profiles, are applied as boundary condition.

Acknowledgements

The authors gratefully acknowledge partial support for this work via the U.S. National Science Foundation (NSF), CMMI - Mechanics of Materials and Structures (MoMS) program grant number 1538332 and CCF - Scalable Parallelism in the Extreme (SPX) program grant number 1725555.

References

[1] T. Kazerani, Effect of micromechanical parameters of microstructure on compressive and tensile failure process of rock, International Journal of Rock Mechanics and Mining Sciences 64 (2013) 44–55.

[2] H. Lan, C. Martin, B. Hu, Effect of heterogeneity of brittle rock on micromechanical extensile behavior during compression loading, Journal of Geophysical Research - Part B - Solid Earth 115 (2010) B01202 (14 pp.).

[3] X. Wang, M. Cai, Modeling of brittle rock failure considering inter- and intra-grain contact failures, Computers and Geotechnics 101 (2018) 224–244.

[4] J. Gallagher Jr, M. Friedman, J. Handin, G. Sowers, Experimental studies relating to microfracture in sandstone, Tectonophysics 21 (3) (1974) 203–247.

[5] C. Fairhurst, N. Cook, The phenomenon of rock splitting parallel to the direction of maximum compression in the neighborhood of a surface, in: Proceedings of the first congress on the international society of rock mechanics, Vol. 1, International Society of Rock Mechanics Lisbon, 1966, pp. 687–692.

[6] W. Brace, B. Paulding Jr, C. Scholz, Dilatancy in the fracture of crystalline rocks, Journal of Geophysical Research 71 (16) (1966) 3939–3953.

[7] J. Li, Debonding of the interface as 'crack arrestor', International Journal of Fracture 105 (1) (2000) 57–79.

[8] X. Zhang, R. G. Jeffrey, M. Thiercelin, Deflection and propagation of fluid-driven fractures at frictional bedding interfaces: A numerical investigation, Journal of Structural Geology 29 (3) (2007) 396–410.

[9] X. Zhang, R. G. Jeffrey, Reinitiation or termination of fluid-driven fractures at frictional bedding interfaces, Journal of Geophysical Research: Solid Earth 113 (B8).

[10] G. Grasselli, A. Lisjak, O. K. Mahabadi, B. S. Tatone, Influence of pre-existing discontinuities and bedding planes on hydraulic fracturing initiation, European Journal of Environmental and Civil Engineering 19 (5) (2015) 580–597.

[11] B. Li, Z. Zhao, Y. Jiang, L. Jing, Contact mechanism of a rock fracture subjected to normal loading and its impact on fast closure behavior during initial stage of fluid flow experiment, International Journal for Numerical and Analytical Methods in Geomechanics 39 (13) (2015) 1431–49.

[12] K. Nolte, et al., A general analysis of fracturing pressure decline with application to three models, SPE Formation Evaluation 1 (06) (1986) 571–583.

[13] J. Bell, Petro geoscience 1. in situ stresses in sedimentary rocks (part 1): measurement techniques, Geoscience Canada 23 (2).

[14] E. J. Nelson, S. T. Chipperfield, R. R. Hillis, J. Gilbert, J. McGowen, S. D. Mildren, The relationship between closure pressures from fluid injection tests and the minimum principal stress in strong rocks, International Journal of Rock Mechanics and Mining Sciences 44 (5) (2007) 787–801.

[15] B. Huang, C. Liu, J. Fu, H. Guan, Hydraulic fracturing after water pressure control blasting for increased fracturing, International Journal of Rock Mechanics and Mining Sciences 48 (6) (2011) 976–83.

[16] T. Mohammadnejad, J. Andrade, Numerical modeling of hydraulic fracture propagation, closure and reopening using XFEM with application to in-situ stress estimation, International Journal for Numerical and Analytical Methods in Geomechanics 40 (15) (2016) 2033–2060.

[17] M. O. Eshkalak, U. Aybar, K. Sepehrnoori, et al., An economic evaluation on the re-fracturing treatment of the US shale gas resources, in: SPE Eastern Regional Meeting, Society of Petroleum Engineers, 2014.

[18] D. Grady, M. Kipp, Continuum modelling of explosive fracture in oil shale, International Journal of Rock Mechanics and Mining Sciences & Geomechanics Abstracts 17 (3) (1980) 147–157.

[19] R. Pramanik, D. Deb, Implementation of smoothed particle hydrodynamics for detonation of explosive with application to rock fragmentation, Rock Mechanics and Rock Engineering 48 (4) (2014) 1683–1698.

[20] J. Page, J. Miskimins, A comparison of hydraulic and propellant fracture propagation in a shale gas reservoir, Journal of Canadian Petroleum Technology 48 (5) (2009) 26–30.

[21] J. V. Lemos, R. D. Hart, P. A. Cundall, A generalized distinct element program for modeling jointed rock mass, in: Int. Proc. Symp. Fundamentals of Rock Joints, 1985, pp. 335–343.

[22] A. Munjiza, D. Owen, N. Bicanic, A combined finite-discrete element method in transient dynamics of fracturing solids, Engineering Computations 12 (2) (1995) 145–174.

[23] A. Munjiza, The Combined Finite-Discrete Element Method, John Wiley & Sons, Chichester, West Sussex, England, 2004.

[24] O. K. Mahabadi, A. Lisjak, A. Munjiza, G. Grasselli, Y-geo: New combined finite-discrete element numerical code for geomechanical applications., International Journal of Geomechanics 12 (6) (2012) 676–688.

[25] A. Munjiza, K. Andrews, NBS contact detection algorithm for bodies of similar size, International Journal for Numerical Methods in Engineering 43 (1) (1998) 131–149.

[26] C. Yan, H. Zheng, G. Sun, X. Ge, Combined finite-discrete element method for simulation of hydraulic fracturing, Rock Mechanics and Rock Engineering 49 (4) (2016) 1389–1410.

[27] C. Yan, Y.-Y. Jiao, A 2D fully coupled hydro-mechanical finite-discrete element model with real pore seepage for simulating the deformation and fracture of porous medium driven by fluid, Computers & Structures 196 (2018) 311–326.

[28] P. Wriggers, T. Vu Van, E. Stein, Finite element formulation of large deformation impact-contact problems with friction, Computers and Structures 37 (3) (1990) 319 – 331.

[29] N. Kikuchi, A smoothing technique for reduced integration penalty methods in contact problems, International Journal for Numerical Methods in Engineering 18 (3) (1982) 343 – 350.

[30] T. Hughes, R. Taylor, J. Sackman, A. Curnier, W. Kanoknukulchai, A finite element method for a class of contact-impact problems, Computer Methods in Applied Mechanics and Engineering 8 (3) (1976) 249 – 276.

[31] J. Simo, P. Wriggers, R. Taylor, A perturbed lagrangian formulation for the finite element solution of contact problems, Computer Methods in Applied Mechanics and Engineering 50 (1985) 163 – 180.

[32] T. Rabczuk, H. Ren, A peridynamics formulation for quasi-static fracture and contact in rock, Engineering Geology 225 (2017) 42–8.

[33] M. Faivre, B. Paul, F. Golfier, R. Giot, P. Massin, D. Colombo, 2D coupled HM-XFEM modeling with cohesive zone model and applications to fluid-driven fracture network, Engineering Fracture Mechanics 159 (2016) 115–143.

[34] P. Papanastasiou, Hydraulic fracture closure in a pressure-sensitive elasto-plastic medium, International Journal of Fracture 103 (2) (2000) 49–161.

[35] F. Cirak, M. West, Decomposition contact response (DCR) for explicit finite element dynamics, International Journal for Numerical Methods in Engineering 64 (8) (2005) 1078 – 1110.

[36] R. Abedi, R. B. Haber, S. Thite, J. Erickson, An h–adaptive spacetime–discontinuous Galerkin method for linearized elastodynamics, Revue Européenne de Mécanique Numérique (European Journal of Computational Mechanics) 15 (6) (2006) 619–42.

[37] R. Abedi, R. B. Haber, Riemann solutions and spacetime discontinuous Galerkin method for linear elastodynamic contact, Computer Methods in Applied Mechanics and Engineering 270 (2014) 150–77.

[38] O. Omidi, R. Abedi, S. Enayatpour, An adaptive meshing approach to capture hydraulic fracturing, in: The 49th US Rock Mechanics/Geomechanics Symposium, San Francisco, California, USA, June 28-July 1, 2015, ARMA 15-572.

[39] O. Allix, A. Corigliano, Modeling and simulation of crack propagation in mixed modes interlaminar fracture, International Journal of Fracture 77 (1996) 111–140.

[40] A. Corigliano, M. Ricci, Rate-dependent interface models: formulation and numerical applications, International Journal of Solids and Structures 38 (1999) 547–576.

[41] G. T. Camacho, M. Ortiz, Computational modelling of impact damage in brittle materials, International Journal of Solids and Structures 33 (1996) 2899–2938.

[42] R. Abedi, R. Haber, Spacetime dimensional analysis and self-similar solutions of linear elastodynamics and cohesive dynamic fracture, International Journal of Solids and Structures 48 (13) (2011) 2076–87.

[43] R. Abedi, A comparative and parametric study of dynamic cohesive and linear elastic fracture mechanics models, International Journal of Solids and Structures 102-103 (2016) 163–75.

[44] N. Mostaghel, T. Davis, Representations of Coulomb friction for dynamic analysis, Earthquake Engineering and Structural Dynamics 26 (5) (1997) 541 – 548.

[45] D. D. Quinn, A new regularization of Coulomb friction, Journal of Vibration and Acoustics, Transactions of the ASME 126 (3) (2004) 391 – 397.

[46] S. Meguid, A. Czekanski, Advances in computational contact mechanics, International Journal of Mechanics and Materials in Design 4 (4) (2008) 419 – 443.

[47] C. Yan, H. Zheng, Three-dimensional hydromechanical model of hydraulic fracturing with arbitrarily discrete fracture networks using finite-discrete element method, International Journal of Geomechanics 17 (6) (2016) 04016133.

[48] P. Gupta, C. A. Duarte, Coupled formulation and algorithms for the simulation of non-planar three-dimensional hydraulic fractures using the generalized finite element method, International Journal for Numerical and Analytical Methods in Geomechanics 40 (10) (2016) 1402–1437.

[49] C. Yan, H. Zheng, A two-dimensional coupled hydro-mechanical finite-discrete model considering porous media flow for simulating hydraulic fracturing, International Journal of Rock Mechanics and Mining Sciences 88 (2016) 115–128.

[50] C. Yan, H. Zheng, FDEM-flow3D: a 3D hydro-mechanical coupled model considering the pore seepage of rock matrix for simulating three-dimensional hydraulic fracturing, Computers and Geotechnics 81 (2017) 212–228.

[51] C. Yan, Y.-Y. Jiao, H. Zheng, A fully coupled three-dimensional hydro-mechanical finite discrete element approach with real porous seepage for simulating 3d hydraulic fracturing, Computers and Geotechnics 96 (2018) 73–89.

[52] P. Gupta, C. Duarte, Simulation of non-planar three-dimensional hydraulic fracture propagation, International Journal for Numerical and Analytical Methods in Geomechanics 38 (13) (2014) 1397–1430.

[53] J. Desroches, E. Detournay, B. Lenoach, P. Papanastasiou, J. Pearson, M. Thiercelin, A. Cheng, The crack tip region in hydraulic fracturing, Proceedings of the Royal Society of London A: Mathematical, Physical and Engineering Sciences 447 (1929) (1994) 39–48.

[54] E. Detournay, Propagation regimes of fluid-driven fractures in impermeable rocks, American Society of Civil Engineers 4 (1) (2004) 35–45.

[55] A. P. Bunger, E. Detournay, D. I. Garagash, Toughness-dominated hydraulic fracture with leak-off, International Journal of Fracture 134 (2) (2005) 175–190.

[56] E. Gordeliy, A. Peirce, Coupling schemes for modeling hydraulic fracture propagation using the {XFEM}, Computer Methods in Applied Mechanics and Engineering 253 (0) (2013) 305–322.

[57] P. Clarke, O. Omidi, R. Abedi, Modeling crack connectivity of induced fractures in a naturally fractured formation, in: Proceeding: 50th US Rock Mechanics/Geomechanics Symposium, Houston, Texas, USA, June 26-29, 2016, ARMA 16-0532.

[58] R. Abedi, R. B. Haber, B. Petracovici, A spacetime discontinuous Galerkin method for elastodynamics with element-level balance of linear momentum, Computer Methods in Applied Mechanics and Engineering 195 (2006) 3247–73.

[59] R. Abedi, S.-H. Chung, J. Erickson, Y. Fan, M. Garland, D. Guoy, R. Haber, J. M. Sullivan, S. Thite, Y. Zhou, Spacetime meshing with adaptive refinement and coarsening, in: Twentieth Annual Symposium on Computational Geometry (SCG '04), Brooklyn, New York, USA, 2004.

[60] R. Abedi, R. B. Haber, P. L. Clarke, Effect of random defects on dynamic fracture in quasi-brittle materials, International Journal of Fracture 208 (1-2) (2017) 241–268.

[61] R. Abedi, O. Omidi, S. Enayatpour, A mesh adaptive method for dynamic well stimulation, Computers and Geotechnics 102 (2018) 12–27.

[62] R. Abedi, M. A. Hawker, R. B. Haber, K. Matouš, An adaptive spacetime discontinuous Galerkin method for cohesive models of elastodynamic fracture, International Journal for Numerical Methods in Engineering 1 (2009) 1–42.

[63] C. Tang, H. Liu, P. Lee, Y. Tsui, L. Tham, Numerical studies of the influence of microstructure on rock failure in uniaxial compression - part I: effect of heterogeneity, International Journal of Rock Mechanics and Mining Sciences 37 (4) (2000) 555–569.

[64] R. Abedi, P. L. Clarke, Modeling of rock inhomogeneity and anisotropy by explicit and implicit representation of microcracks, in: Proceeding: 52nd US Rock Mechanics/Geomechanics Symposium, Seattle, Washington, USA, June 17-20, 2018, ARMA 18-151-0228-1094.

[65] R. Abedi, R. Haber, A. Elbanna, Mixed-mode dynamic crack propagation in rocks with contact-separation mode transitions, in: Proceeding: 51th US Rock Mechanics/Geomechanics Symposium, San Francisco, California, USA, June 25-28, 2017, ARMA 17-0679.

[66] R. Abedi, O. Omidi, P. Clarke, A numerical study on the effect of loading and randomness on fracture patterns in a tight formation, in: Proceeding: 51th US Rock Mechanics/Geomechanics Symposium, San Francisco, California, USA, June 25-28, 2017, ARMA 17-0641.